CLOSED ANALYTICAL FORMULAE FOR MULTI-POLE MAGNETIC RINGS

U. Ausserlechner[*]

Infineon Technologies Austria AG, Siemensstrasse 2, Villach 9500, Austria

Abstract—Multi-pole permanent magnetic encoders are used for wheel speed sensing in automotive systems. This paper discusses rings and discs magnetized along axial direction. The vector field is calculated analytically in 3D as sums over all poles. For the case of discs with vanishing inner and infinite outer diameter the summation is done in closed form with a new summation formula. The results are discussed and several plots of field patterns are given in normalized form: At very small air-gap the field shows an overshoot. At moderate and large air-gaps it is a sine-function with exponentially decaying amplitude. The amplitude versus air gap, reading radius, thickness of the magnetic layer, and number of poles is studied and excellent agreement with measurements is found. The effect of a steel-back on the field is explained. It is also shown how to maximize the torque transmitted in axially magnetized couplings.

1. INTRODUCTION

Active target wheels are used in automotive systems for position and speed sensing [1–5]. These are rings fixed to a shaft, whose angular position or velocity should be converted into an electronic signal [6, 7]. Also small drives use these miniature encoders to control the rotation of the shaft [8]. To this end a large number of small permanent magnets resides along their circumference. They produce a magnetic field which is periodic with respect to the angle of rotation. When the shaft rotates the periodic magnetic field of the code wheel passes a magnetic field sensor, which is attached to the stator frame. The sensor converts these apparent oscillations of the magnetic field into digital

pulses of an electronic output signal. During operation several effects like tolerances, deformation under load, wear and the slackness of the bearing cause changes in distance between the code wheel and the sensor. Therefore it is necessary to investigate the field distribution around the nominal position of the sensor in order to adjust its threshold levels with reasonable room for tolerances.

Several authors have calculated the magnetic field pattern of multi-pole magnetic encoder wheels [9–11], radially polarized cylinders [12], axially polarized multi-pole discs [13, 14], and tile magnets with tangential polarization [15, 16]. They have derived equations for the field resulting from one pole and then summed up the contributions of all poles numerically. This procedure is apt to analyze a particular setup. Yet it is less suited to understand the intricate dependencies of all involved parameters, because it does not provide a closed form equation of the field pattern.

Periodic permanent magnets or current grids are also used for surface containment of plasmas (e.g., Tokamaks for nuclear fusion research). The magnetic fields of these structures were expressed as rapidly converging Fourier series [17, 18], series with Bessel functions [19] and in closed form [20, 21]. Two-dimensional confinement systems for ion sources were calculated in [22]. For boundary layer control in magnetohydrodynamics similar arrangements of magnets were investigated with conformal mapping [23, 24]. The 2D case of an azimuthally magnetized multi-pole drum for magnetic separators was treated in closed form [25]. Axial flux permanent-magnet generators and motors and magnetic torque transducers use similar configurations [26–28].

This work derives analytical field calculations in 3D for discs with axially magnetized segments. First the field of a single pole is calculated and then the contributions of all poles are summed up. It is possible to compute the sum over all poles in closed form. This gives a highly nonlinear equation that provides insight into the structure of the magnetic field of such multipoles. The limit of vanishing curvature where the disc becomes a linear strip is also investigated.

2. DEFINITIONS

For the mathematical treatment of the magnetic field of code wheels according to Fig. 1 a cylindrical coordinate system (r, ψ, z) with unit vectors $(\vec{n}_r, \vec{n}_\psi, \vec{n}_z)$ is used. The z-axis is identical with the axis of rotation of the shaft onto which the code wheel is mounted. The permanent magnetic part of the code wheel consists of a ring with inner diameter $2r_1$ and outer diameter $2r_2$, having a width $w = r_2 - r_1$. The
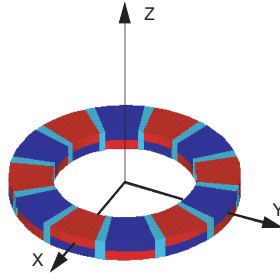
Figure 1. A multi-pole magnetic encoder ring for wheel speed sensing: The ring is composed of $2p$ segments (drawn for $p = 6$) of thickness t in z-direction arranged on the circumference of a ring with inner diameter $2r_1$ and outer diameter $2r_2$. Each of the segments is magnetized in z-direction, however with alternating sign for neighboring segments. Between two magnetized regions there is a slim wedge, where the material is not magnetized. An idealized model assumes that the ring degenerates to a disc (i.e., the inner diameter vanishes and the outer diameter extends to infinity).

ring is made up of $2p$ segments, each covering an azimuthal angle

$$\psi_{k,1} \leq \psi \leq \psi_{k,3}, \quad 0 \leq k \leq 2p - 1, \tag{1}$$

$$\psi_{k,1} = -\pi/(2p) + \delta/2 + \pi k/p = \pi\left(-1 + lf + 2k\right)/\left(2p\right), \tag{2a}$$

$$\psi_{k,3} = \pi/(2p) - \delta/2 + \pi k/p = \pi\left(1 - lf + 2k\right)/\left(2p\right). \tag{2b}$$

Since the p pole pairs are symmetrically arranged the field pattern exhibits an azimuthal period of $2\pi/p$. Therefore it is sufficient to plot the field in the interval $-\pi/p \leq \psi \leq \pi/p$. Instead of the azimuthal angel ψ it is common practice to use the distance on the perimeter $r\psi$ as linear coordinate of the field pattern. Here r is the reading radius: it denotes the distance of the magnetic field sensor from the rotation axis. The spatial period is equal to the size of one north-pole plus one south-pole plus two non-magnetic wedges $\lambda = 2\pi\, r/p$. An angel δ separates two adjacent regions of magnetization, where the material is not polarized. This diluting effect is described by the loss factor $lf = p\,\delta/\pi$; e.g., $lf = 0.07$ means that 7% of the circumference of the code wheel is not magnetized. In axial direction the code wheel has a thickness t and extends from $-t/2 \leq z \leq t/2$. The magnetic field sensor is placed at a distance $g = z - t/2$ above the wheel: this is called the air-gap. In this work we focus on code wheels with magnetization in axial direction $\vec{M}_k = (-1)^k M \vec{n}_z$.

3. THE EQUIVALENT CURRENT SHEET APPROACH

First the field generated by the k-th segment $\vec{B}_k^{\text{ring}}$ is computed and then the field $\vec{B}^{\text{ring}}$ of the complete encoder is derived by superposition of all $2p$ segments:

$$\vec{B}^{\text{ring}} = \sum_{k=0}^{2p-1} \vec{B}_k^{\text{ring}}. \tag{3}$$

Plain superposition is allowed as long as the code wheel is permanent magnetic with large coercivity. The magnetization $\vec{M}_k$ is replaced by an equivalent current density $\vec{S}_k$, according to the rule $\vec{S}_k = \vec{\nabla} \times \vec{M}_k$ [29] and the small permeability[†] of the permanent magnetic material is neglected. The field calculation is simplified by the fact that the magnetization throughout the segment is homogeneous, so that there is no equivalent current density within the segment (because the curl of the magnetization vanishes there). One only has to account for a current layer of constant current density on these parts of the surface, which are parallel to the direction of the magnetization. Applying $\vec{S}_k = \vec{\nabla} \times \vec{M}_k$ to the surface of the permanent magnetic segment gives $\vec{\alpha}_k = -\vec{n}_k \times \vec{M}_k$, where $\vec{\alpha}_k$ is the equivalent current layer density, and $\vec{n}_k$ is the unit vector perpendicular to the surface and pointing outside of the magnetized volume. Hence, the relevant surface of the k-th segment can be decomposed into four parts $A_{k,1}$ to $A_{k,4}$, which are

$$A_{k,1} : \left(\psi' = \psi_{k,1}, r_1 \leq r' \leq r_2, -t/2 \leq z' \leq t/2 \right), \tag{4a}$$

$$\vec{n}_k = -\vec{n}_{\psi'}, \; \vec{\alpha}_{k,1} = (-1)^k M \vec{n}_{r_{k,1}}, \; \vec{n}_{r_{k,1}} = \cos\psi_{k,1}\vec{n}_x + \sin\psi_{k,1}\vec{n}_y \tag{4b}$$

$$A_{k,2} : \left(\psi_{k,1} \leq \psi' \leq \psi_{k,3}, r' = r_2, -t/2 \leq z' \leq t/2 \right), \tag{4c}$$

$$\vec{n}_k = \vec{n}_{r'}, \; \vec{\alpha}_{k,2} = (-1)^k M \vec{n}_\psi \tag{4d}$$

$$A_{k,3} : \left(\psi' = \psi_{k,3}, r_1 \leq r' \leq r_2, -t/2 \leq z' \leq t/2 \right), \tag{4e}$$

$$\vec{n}_k = \vec{n}_{\psi'}, \; \vec{\alpha}_{k,3} = -(-1)^k M \vec{n}_{r_{k,3}}, \; \vec{n}_{r_{k,3}} = \cos\psi_{k,3}\vec{n}_x + \sin\psi_{k,3}\vec{n}_y \tag{4f}$$

$$A_{k,4} : \left(\psi_{k,1} \leq \psi' \leq \psi_{k,3}, r' = r_1, -t/2 \leq z' \leq t/2 \right), \tag{4g}$$

$$\vec{n}_k = -\vec{n}_{r'}, \; \vec{\alpha}_{k,4} = -(-1)^k M \vec{n}_{\psi'} \tag{4h}$$

where primed coordinates (r', ψ', z') are used to distinguish the source points $\vec{r}'$ from the test points $\vec{r} = (r, \psi, z)$. The total field generated by the k-th segment is the sum of the fields of the four sheet current densities $\vec{\alpha}_{k,1}$ to $\vec{\alpha}_{k,4}$:

$$\vec{B}_k^{\text{ring}} = \vec{B}_{k,1}^{\text{ring}} + \vec{B}_{k,2}^{\text{ring}} + \vec{B}_{k,3}^{\text{ring}} + \vec{B}_{k,4}^{\text{ring}}. \tag{5}$$

[†] For NdFeB magnets with a remanence of 1.2T and a coercivity HcB $= 900\,\text{kA/m}$ the relative permeability is $1.2/(4*\pi*10^\wedge-7*9*10^\wedge5) = 1.06$.

4. THE FIELD OF A SINGLE POLE OF AN AXIALLY MAGNETIZED MULTI-POLAR RING

The induction field of the equivalent currents of the k-th pole is computed by the law of Biot-Savart. For $\vec{\alpha}_{k,1}$ this gives

$$\vec{B}_{k,1}^{\text{ring}}(\vec{r}) = (-1)^k \frac{B_{rem}}{4\pi} \int\limits_{r'=r_1}^{r_2} \int\limits_{z'=-t/2}^{t/2} \frac{\vec{n}_{r_{k,1}} \times (\vec{r} - \vec{r}')}{|\vec{r} - \vec{r}'|^3} \, dz' dr' \quad (6)$$

with the remanence $B_{rem} = \mu_0 M$. The result is

$$\vec{B}_{k,1}^{\text{ring}}(\vec{r}) = \vec{V}(\psi - \psi_{k,1}, z + t/2, r_2) - \vec{V}(\psi - \psi_{k,1}, z - t/2, r_2)$$
$$-\vec{V}(\psi - \psi_{k,1}, z + t/2, r_1) + \vec{V}(\psi - \psi_{k,1}, z - t/2, r_1) \quad (7a)$$

$$\vec{n}_r \cdot \vec{V}(\varphi, \zeta, \rho) = \tan\varphi \, \vec{n}_\psi \cdot \vec{V}(\varphi, \zeta, \rho) \quad (7b)$$

$$\vec{n}_\psi \cdot \vec{V}(\varphi, \zeta, \rho)$$
$$= (-1)^k \cos\varphi \frac{B_{rem}}{8\pi} \ln \frac{\sqrt{\zeta^2 + \rho^2 + r^2 - 2r\rho\cos\varphi} + (\rho - r\cos\varphi)}{\sqrt{\zeta^2 + \rho^2 + r^2 - 2r\rho\cos\varphi} - (\rho - r\cos\varphi)} \quad (7c)$$

$$\vec{n}_z \cdot \vec{V}(\varphi, \zeta, \rho) = (-1)^k \frac{B_{rem}}{4\pi} \arctan \frac{\zeta(\rho - r\cos\varphi)}{r\sin\varphi \sqrt{\zeta^2 + \rho^2 + r^2 - 2r\rho\cos\varphi}} \quad (7d)$$

The field contribution of $\vec{\alpha}_{k,3}$ is computed by replacing B_{rem} with $-B_{rem}$ and $\psi_{k,1}$ with $\psi_{k,3}$. Integration over the current layers $\vec{\alpha}_{k,2}$ and $\vec{\alpha}_{k,4}$ in azimuthal direction leads to incomplete elliptic integrals. It will be shown that in many cases of practical interest these contributions can be neglected.

5. THE FIELD OF ONE POLE OF AN AXIALLY MAGNETIZED MULTI-POLAR DISC

If the inner diameter vanishes and the outer diameter moves to infinity the contribution of the azimuthal sheet currents $\vec{\alpha}_{k,2}$ and $\vec{\alpha}_{k,4}$ to the resulting field becomes zero.

$$\vec{B}_k^{\text{disc}} = \lim_{r_1 \to 0, \, r_2 \to \infty} \vec{B}_k^{\text{ring}} = \vec{B}_{k,1}^{\text{disc}} + \vec{B}_{k,3}^{\text{disc}}$$
$$\text{with} \quad \lim_{r_1 \to 0, \, r_2 \to \infty} \vec{B}_{k,1}^{\text{ring}} = \vec{B}_{k,1}^{\text{disc}}, \quad \lim_{r_1 \to 0, \, r_2 \to \infty} \vec{B}_{k,3}^{\text{ring}} = \vec{B}_{k,3}^{\text{disc}}. \quad (8)$$

The radial and azimuthal components of $\vec{V}(\varphi, z + t/2, r_2) - \vec{V}(\varphi, z - t/2, r_2)$ converge to a finite value in the limit $r_2 \to \infty$ although both single terms $\vec{V}(\varphi, z + t/2, r_2)$, $\vec{V}(\varphi, z - t/2, r_2)$ diverge.

Hence, the field of one pole of a disc is given by

$$\vec{n}_r \cdot \vec{B}_{k,1}^{\text{disc}} = \tan\left(\psi - \psi_{k,1}\right) \vec{n}_\psi \cdot \vec{B}_{k,1}^{\text{disc}} \tag{9a}$$

$$\vec{n}_\psi \cdot \vec{B}_{k,1}^{\text{disc}} = \cos\left(\psi - \psi_{k,1}\right)(-1)^k \frac{B_{rem}}{4\pi}$$

$$\ln \frac{\sqrt{(|z|-t/2)^2+r^2} - r\cos(\psi-\psi_{k,1})}{\sqrt{(|z|+t/2)^2+r^2} - r\cos(\psi-\psi_{k,1})} \tag{9b}$$

$$\vec{n}_z \cdot \vec{B}_{k,1}^{\text{disc}} = (-1)^k \frac{B_{rem}}{4\pi} \{f_1(\zeta, \psi - \psi_{k,1}) + f_2(\zeta, \psi - \psi_{k,1})\}\Big|_{\zeta=(|z|-t/2)/r}^{(|z|+t/2)/r} \tag{9c}$$

$$f_1\left(\zeta, \varphi\right) = \arctan\left(\zeta/\sin\varphi\right), \tag{9d}$$

$$f_2\left(\zeta, \varphi\right) = \arctan\left(\zeta \cot\varphi/\sqrt{1+\zeta^2}\right) \tag{9e}$$

with the abbreviation $f(b) - f(a) = f(x)|_{x=a}^b$.

6. CLOSED FORMS FOR THE SUMS OVER ALL POLES

6.1. The Axial Field Component of Multi-polar Discs

With (1)–(3), (8), and (9c)–(9e) a closed form expression for the axial field of code discs with $2p$ poles is obtained

$$B_z^{\text{disc}} = \sum_{k=0}^{2p-1} \vec{n}_z \cdot \left(\vec{B}_{k,1}^{\text{disc}} + \vec{B}_{k,3}^{\text{disc}}\right). \tag{10}$$

By use of the equation (cf. Appendix A)

$$\sum_{k=0}^{2p-1} (-1)^k \left(f_1\left(\zeta, \varphi - \pi k/p\right) + f_2\left(\zeta, \varphi - \pi k/p\right)\right) = 2\arctan\left(\frac{\text{Sh}(\zeta; p)}{\sin\left(p\varphi\right)}\right) \tag{11}$$

with $\text{Sh}\left(\zeta; p\right)$ as defined in Appendix B, one gets

$$B_z^{\text{disc}} = \frac{B_{rem}}{2\pi} \sum_{\bar{\psi}} \arctan\left(\frac{\text{Sh}\left(\zeta; p\right)}{\cos\bar{\psi}}\right)\Bigg|_{\zeta=(z-t/2)/r}^{(z+t/2)/r} \tag{12a}$$

where the sum is taken over the two values $\bar{\psi} = p\psi + \pi lf/2$ and $\bar{\psi} = p\psi - \pi lf/2$. In other words

$$B_z^{\text{disc}} = \frac{B_{rem}}{2\pi} \sum_{\bar{\psi}} \arctan\left[\frac{\cos\bar{\psi}[\text{Sh}\left((z+t/2)/r; p\right) - \text{Sh}\left((z-t/2)/r; p\right)]}{(\cos\bar{\psi})^2 + \text{Sh}\left((z+t/2)/r; p\right)\text{Sh}\left((z-t/2)/r; p\right)}\right] \tag{12b}$$

Equations (12a) and (12b) show the periodicity of the field pattern $2\pi/p$. For $\delta = 0$ or $\psi = 0$ (12b) collapses to a single term. Fig. 2
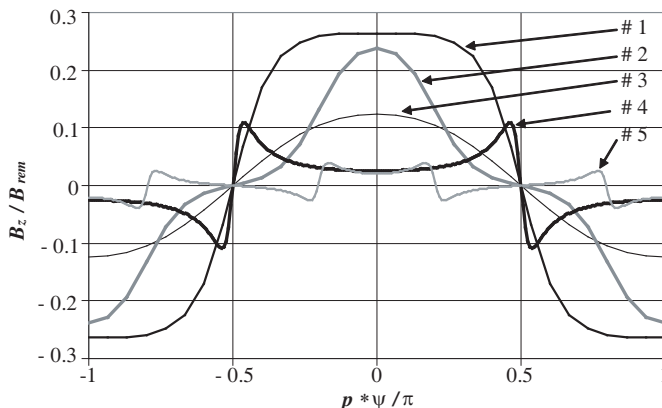
Figure 2. Axial field for various cases. Thickness and radius are equal for all cases: 1 mm and 25 mm, respectively. Number of poles, air-gap and loss factor vary according to the table.

Case	# 1	# 2	# 3	# 4	# 5
p	33	34	32	2	1
g [mm]	0.3	0.3	1.0	1.0	2.0
lf	0	0.6	0	0	0.6

shows the field profile for various cases: # 3 is harmonic for moderate and large z. In contrast to this, # 1 shows the profile for small z and $\delta = 0$. # 2 is for small z and $lf = 0.6$. # 4 shows the field of a disc with only two pole pairs and zero loss factor: it has significant overshoot. # 5 shows the pattern for a disc with only 1 north- and 1 south-pole with $lf = 0.6$. The curves with overshoot have smaller amplitudes than curves without overshoot.

The limit of vanishing air-gap $|z| \rightarrow t/2$ is readily calculated by (12a). This shows that the field on the surface of the disc increases with increasing number of poles, even though each pole becomes smaller. Fig. 3 shows that for large pole count the field amplitude at $\psi = 0$ for vanishing air-gap saturates at half of the remanent field, whereby this trend is accelerated in the dilute limit $\delta \rightarrow \pi/p$, i.e., $lf \rightarrow 1$, when the various magnetic poles do not interact notably any more. This is analogous to the field on top of an axially magnetized cylindrical magnet, which increases with decreasing diameter until its maximum value of half of the remanence, when the magnet degenerates to a needle.
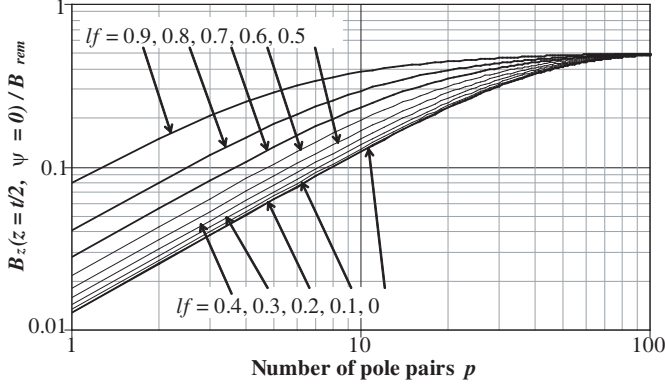
Figure 3. Magnetic field above the center of a north pole ($\psi = 0$) on the surface of a code-wheel versus number of pole-pairs (various loss factors, $t/r = 1/15$). With large number of poles the field approaches half of the remanence. For small number of poles the field magnitude directly above the center-line of a pole decreases. With growing loss factor — i.e., smaller magnetized segments — the field magnitude in the center of the segment increases.

Near the z-axis the field is small of the order r^p

$$\lim_{r \to 0} B_z^{\text{disc}} = \frac{2B_{rem}}{\pi} \left(r \operatorname{sgn} z \right)^p \left((2z-t)^{-p} - (2z+t)^{-p} \right) \cos\left(\frac{\delta}{2}\right) \cos p\,\psi \quad (13)$$

with $\operatorname{sgn} z = z/|z|$. Contrarily the field decays only of the order $1/r$ for large reading radius. The maximum B_z versus rotational position ψ is called the amplitude $\hat{B}_z$ and occurs at $\hat{\psi}_z$. For $lf = 0$ the amplitudes are obtained by differentiating (12a) versus ψ and equating the result to zero. There is always a relative extreme $\hat{B}_z^{(\text{no})}$ at $\psi = 0$, π/p, $2\pi/p \ldots$ with

$$\hat{B}_z^{(\text{no})} = B_z^{\text{disc}} \left(\psi = 0 \right) = \frac{B_{rem}}{\pi} \left\{ \arctan\left[\operatorname{Sh}\left(\frac{2z+t}{r}; p\right) \right] - \arctan\left[\operatorname{Sh}\left(\frac{2z-t}{r}; p\right) \right] \right\} (14a)$$

Yet only for moderate and large air-gaps this is equal to the amplitude (cf. Fig. 2: #1, 2, 3). At very small air-gaps g the B_z-field exhibits overshoot $\hat{B}_z^{(\text{os})} \geq \hat{B}_z^{(\text{no})}$ as shown in Fig. 2: #4, 5, at rotational position $\hat{\psi}_z$: $\left(\cos\left(p\hat{\psi}_z \right) \right)^2 = \operatorname{Sh}\left((g+t)/r; p \right) \operatorname{Sh}\left(g/r; p \right)$. The overshoot amplitude is

$$\hat{B}_z^{(\text{os})} = B_z^{\text{disc}} \left(\psi = \bar{\psi}_z \right)$$

$$= \frac{B_{rem}}{\pi} \left\{ \arctan\sqrt{\frac{\operatorname{Sh}((z+t/2)/r; p)}{\operatorname{Sh}((z-t/2)/r; p)}} - \arctan\sqrt{\frac{\operatorname{Sh}((z-t/2)/r; p)}{\operatorname{Sh}((z+t/2)/r; p)}} \right\} (14b)$$

The required condition for overshoot is $\mathrm{Sh}\,((g+t)/r;p)\,\mathrm{Sh}\,(g/r;p) \leq 1$, which by use of (B10) is identical to $(g+t)/r \leq \mathrm{Sh}\,(1/\mathrm{Sh}\,(g/r;p);1/p)$. With (B12) we obtain a limit curve which separates the regime of overshoot of B_z from the regime of non-overshoot:

$$\frac{t}{r} \leq \sinh\left\{\frac{-1}{p}\ln\left[\tanh\left(\frac{p}{2}\mathrm{arcsinh}\frac{g}{r}\right)\right]\right\} - \frac{g}{r} \tag{15a}$$

Figure 4 shows this limit curve in the pg/r-pt/r-plane: Although strictly speaking the limit curve depends on p it converges rapidly for large p, so that we may use the limit of $p \to \infty$ except for $p = 1, 2, 3$:

$$\frac{pt}{r} \leq -\ln\left(\tanh\frac{pg}{2r}\right) - \frac{pg}{r} \approx -\ln\frac{pg}{2r} - \frac{pg}{r} \tag{15b}$$

Thus, overshoot $\hat{B}_z^{(\mathrm{os})}$ is limited to small t and small g. Even if t vanishes there is no $\hat{B}_z^{(\mathrm{os})}$ for $pg/r > 0.8814\ldots 1.0$ (depending on p, cf. Fig. 4).

For practically all sensors and most magnetic coupling applications it holds $|z|+t/2 \ll r$ so that we can approximate $\mathrm{Sh}\,(\zeta;p) \to \sinh p\,\zeta$ in
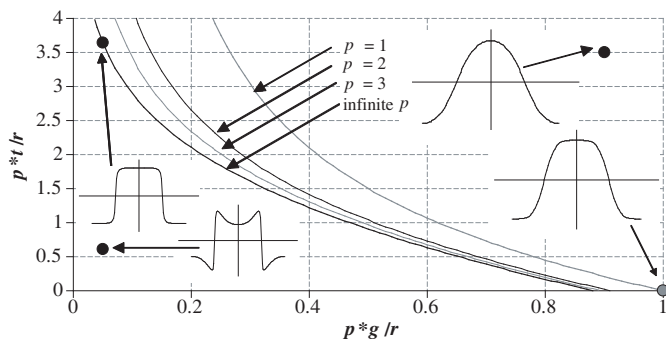

Figure 4. Limit curves (15a) for various p in the $(pg/r;pt/r)$-plane. Above the limit curves the $B_z(\psi)$ patterns exhibit no overshoot; below them there is overshoot. Four discs with specific parameters $(pg/r; pt/r)$ are denoted by points. The gray point at $pg/r = 1$ corresponds to $p = 1$. The black points are for infinitely large p. The corresponding $B_z(\psi)$ patterns are given as insets. Thin discs with very small air-gaps are represented by points below the limit curve: they exhibit overshoot. Thick discs at moderate and large air-gaps correspond to points above the limit curve: they have sinusoidal $B_z(\psi)$ patterns. Points on the limit curve have flat peaks: there the second derivative of $B_z(\psi)$ vanishes. If the points move on the limit curves to the left this leads to rectangular pulse shapes.

(12a) and (12b) (cf. (B14)). For zero loss factor the overshoot $\hat{B}_z^{(os)} \geq$ $\hat{B}_z^{(no)}$ occurs at $\hat{\psi}_z$ with $\cos\left(2p\hat{\psi}_z\right) = \cosh\left(2pz/r\right) - \cosh\left(pt/r\right) - 1$:

$$\hat{B}_z \cong \begin{cases} \hat{B}_z^{(os)} \ldots [1 - \sinh\left(pg/r\right)]/\cosh\left(pg/r\right) \leq \tanh\left(pt/(2r)\right) \\ \hat{B}_z^{(no)} \ldots [1 - \sinh\left(pg/r\right)]/\cosh\left(pg/r\right) \geq \tanh\left(pt/(2r)\right) \end{cases} \quad (16a)$$

$$\hat{B}_z^{(os)} = \hat{B}_z\left(\psi = \hat{\psi}_z\right) = \frac{B_{rem}}{\pi} \arctan \frac{\sqrt{2}\cosh\left(pz/r\right)\sinh\left(pt/(2r)\right)}{\sqrt{\cosh\left(2pz/r\right) - \cosh\left(pt/r\right)}} \quad (16b)$$

$$\hat{B}_z^{(no)} = \hat{B}_z\left(\psi = 0\right) = \frac{B_{rem}}{\pi} \arctan \frac{4\cosh\left(pz/r\right)\sinh\left(pt/(2r)\right)}{2 + \cosh\left(2pz/r\right) - \cosh\left(pt/r\right)} \quad (16c)$$

(16b) grows monotonically versus p, yet (16c) shows a relative maximum versus p. Similar findings are reported in [30] and this will become important in Section 10.

   Figure 5 compares both amplitudes versus normalized air-gap $p\,g/r$. Unless the air-gap is not extremely small we may also neglect the $\cos^2$-term in the denominator of (12b). For moderate and large air-gaps we may skip the artcan-evaluation, as long as $10\sinh\left(p\,t/(2r)\right)\cosh\left(pz/r\right) \ll \cosh\left(2p\,z/r\right)$ holds.

   Finally one obtains a simple exponential decay versus air-gap

$$B_z^{disc} \approx 2pt\frac{B_{rem}}{\pi r}\cos\frac{p\,\delta}{2}\exp\left(\frac{-p\,|z|}{r}\right)\cos\left(p\psi\right) \quad (17)$$
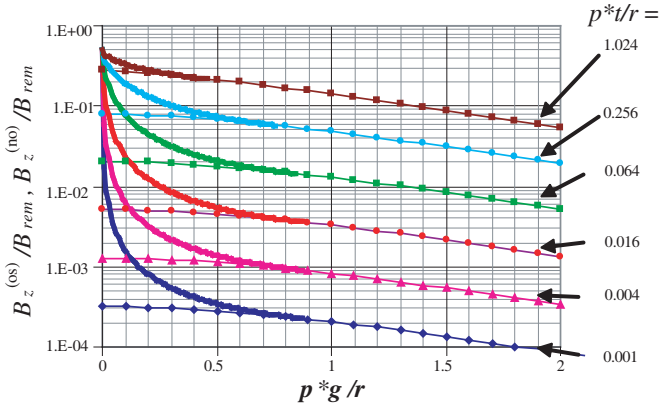

Figure 5. Amplitudes $\hat{B}_z^{(no)}$ without overshoot (thin lines with symbols) and $\hat{B}_z^{(os)}$ with overshoot (thick lines). Pronounced overshoot is observed for thin discs $t \ll r/p$. $\hat{B}_z^{(os)}$ tends to $B_{rem}/2$ at vanishing air-gap.
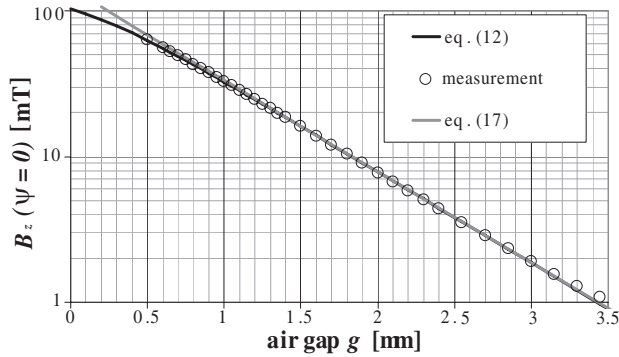
Figure 6. Amplitude of magnetic field B_z of a code-wheel versus magnetic air-gap: comparison of measurement and calculation. The open circles represent measurements on the encoder seal JT65 from SNR Roulements (France) with the following data: 44 pole pairs, $t = 1\,\text{mm}$, $r_1 = 28.75\,\text{mm}$, $r_2 = 32.85\,\text{mm}$, the permeable steel supporting ring is 0.5 mm thick. The field was measured with a Gaussmeter, which was positioned at a reading radius $r = 31.2\,\text{mm}$. This measurement shows that the model of a code disc approximates the field of a real code wheel with steel back sufficiently accurately.

The exponential decay of the field versus air-gap is known empirically [1, 2] and theoretically [23] since a long time. With (12) and (17) it becomes apparent how this exponential law develops from a multi-pole of order p in the limit $|z| \ll r$.

Figure 6 compares measurements with the exact field solution from (12) and the approximate one of (17): the simplified model of a disc approximates the axial magnetic field of realistic encoders accurately enough for most applications. Thereby the code ring under investigation was mounted on a thin steel support ring, which is highly permeable. For air-gaps which are smaller than the width of the ring $|z| \leq w$ the steel ring can be replaced by an infinite plane, which is mathematically accounted for by current images [31].

The far field of the disc is obtained by $|z| \gg r$.

$$\lim_{z \to \infty} B_z^{\text{disc}} = 2pt \frac{B_{rem}}{\pi z} \cos \frac{p\,\delta}{2} \left(\frac{2\,|z|}{r} \right)^{-p} \cos(p\psi) \tag{18}$$

It shows that the arrangement is a multipole of order p.

In the limit of $t \to 0$ the B_z-pattern of (12a) becomes

$$\lim_{t \to 0} B_z^{\text{disc}} = \frac{pt B_{rem}}{2\pi \sqrt{z^2 + r^2}} \sum_{\bar\psi} \frac{\text{Ch}\,(z/r; p) \cos \bar\psi}{\cos^2 \bar\psi + \text{Sh}^2\,(z/r; p)} \tag{19}$$

6.2. The Radial Field Component of Multi-polar Discs

For infinitely thin discs (9a) reads

$$\lim_{t\to 0} \vec{n}_r \cdot \vec{B}_{k,1}^{\text{disc}} = \frac{-B_{rem}t}{4\pi r} \frac{|z|}{\sqrt{r^2+z^2}} \frac{(-1)^k \sin\left(\psi-\psi_{k,1}\right)}{\sqrt{1+(z/r)^2-\cos\left(\psi-\psi_{k,1}\right)}} \tag{20}$$

$B_{rem} \to \infty$ while $t \to 0$ so that their product remains constant. With [32] one can sum up all terms in closed form. This is repeated for $\vec{\alpha}_{k,3}$ and finally leads to

$$\lim_{t\to 0} B_r^{\text{disc}} = \frac{-B_{rem}tp}{2\pi r\sqrt{r^2+z^2}} \sum_{\bar{\psi}} \frac{|z|\,\text{Ch}\left(|z|/r;p\right)\cos\bar{\psi}}{\text{Sh}^2\left(|z|/r;p\right)+\cos^2\bar{\psi}} \tag{21}$$

The sum over $\bar{\psi}$ is like in (12a). (21) is also obtained from (12) in the limit $t \to 0$ by the relation $\partial B_r/\partial z = \partial B_z/\partial r$ (vanishing curl). Thus B_r- and B_z-fields are related by (19) and (21).

$$r\lim_{t\to 0} B_r = -|z|\lim_{t\to 0} B_z \tag{22}$$

At moderate and large z and for $lf = 0$ the B_r-field has its amplitude at $0°$: $B_r\left(\psi = 0\right) = \hat{B}_r^{(\text{no})}$. For very small z and $lf = 0$ the B_r-field exhibits an overshoot: $B_r\left(\psi = \hat{\psi}_r\right) = \hat{B}_r^{(\text{os})} > \hat{B}_r^{(\text{no})}$ with $\hat{\psi}_r = \arccos\left(\text{Sh}\left(|z|/r;p\right)\right)$. Comparison with Section 6.1 shows that B_z-field and B_r-field have their maxima and overshoot at same angular positions $\hat{\psi}_r = \hat{\psi}_z$ and also the same limit curve $\text{Sh}\left(|z|/r;p\right) = 1$ applies (due to (22)). With (B10) the limit curve can also be given explicitly $|z|/r = \text{Sh}\left(1;1/p\right)$. The amplitudes are

$$\lim_{t\to 0} \hat{B}_r^{(\text{os})} = \frac{|z|}{r}\lim_{t\to 0} \hat{B}_z^{(\text{os})} = \frac{B_{rem}pt}{\pi r} \frac{|z|}{\sqrt{r^2+z^2}} \frac{1}{2}\frac{\text{Ch}\left(|z|/r;p\right)}{\text{Sh}\left(|z|/r;p\right)} \tag{23a}$$

$$\lim_{t\to 0} \hat{B}_r^{(\text{no})} = \frac{|z|}{r}\lim_{t\to 0} \hat{B}_z^{(\text{no})} = \frac{B_{rem}pt}{\pi r} \frac{|z|}{\sqrt{r^2+z^2}} \frac{1}{\text{Ch}\left(|z|/r;p\right)} \tag{23b}$$

It is interesting to study the z-dependence of (23):

$$\lim_{z\to 0}\lim_{t\to 0} \hat{B}_r^{(\text{os})} = B_{rem}t/(2\pi r) \quad\text{and}\quad \lim_{z\to 0}\lim_{t\to 0} \hat{B}_r^{(\text{no})} = 0 \tag{24}$$

Starting at $z = 0$ $\hat{B}_r^{(\text{os})}$ does not vanish whereas $\hat{B}_r^{(\text{no})}$ vanishes. Then, for growing z-distance both amplitudes grow! $\hat{B}_r^{(\text{os})}$ attains its maximum at the limit curve $|z|/r = \text{Sh}\left(1;1/p\right)$:

$$\lim_{t\to 0} \hat{B}_r^{(\text{os})} \le \frac{B_{rem}t}{\pi r} \frac{p}{\sqrt{2}}\frac{\text{Sh}\left(1;1/p\right)}{\text{Ch}\left(1;1/p\right)} \quad \text{for } 0 < |z| < r\,\text{Sh}\left(1;1/p\right) \tag{25}$$

$\hat{B}_r^{(no)}$ grows even further until a maximum is reached at $z_{\max}$ defined by the equation

$$p\frac{|z_{\max}|}{r}\sqrt{1+(z_{\max}/r)^2}\frac{\mathrm{Sh}\left(|z_{\max}|/r;p\right)}{\mathrm{Ch}\left(|z_{\max}|/r;p\right)}=1 \qquad (26)$$

The solution is $pz_{\max}/r=1$ for $p=1$, $pz_{\max}/r=1.11179$ for $p=2$, and $pz_{\max}/r=1.19968$ for large p. The amplitude is

$$\lim_{t\to 0}\hat{B}_r^{(no)}\left(z=z_{\max}\right)=(1.0\ldots 1.32549)\frac{B_{rem}t}{2\pi r} \qquad (27)$$

where the factor 1.0 applies for $p=1$, and the factor 1.32549 applies for large p.

Near the rotation axis $\hat{B}_r^{(os)}$ is not defined, since it must hold $|z|/r \leq \mathrm{Sh}\left(1;1/p\right)$. Thus there is no overshoot near the rotation axis. However $\hat{B}_r^{(no)}$ is defined there and it diminishes like $(r/|z|)^{p-1}\big/\sqrt{r^2+z^2}$. At large radial distance the B_r-field diminishes like r^{-2}. Thus for $p>1$ there must be a maximum at intermediate radial distances[‡], which can be found by differentiation $\partial\hat{B}_r^{(no)}\left(r=r_{\max}\right)\big/\partial r=0$. This gives

$$p\frac{|z|}{r_{\max}}\sqrt{1+(z/r_{\max})^2}\frac{\mathrm{Sh}\left(|z|/r_{\max};p\right)}{\mathrm{Ch}\left(|z|/r_{\max};p\right)}=2+(z/r_{\max})^2 \qquad (28)$$

the solution of which is $p\,|z|/r_{\max}=2.2634$ for $p=2$ and decreases to 2.0653 for large p.

For $p\zeta>1\gg\zeta$ it holds $\mathrm{Ch}\left(\zeta;p\right)\to\exp\left(p\,\zeta\right)/2$. Integration of (21) over the thickness gives

$$B_r^{disc}\to\frac{-2B_{rem}p\,t\,|z|}{\pi\,r^2}\cos\left(\frac{\pi lf}{2}\right)\exp\left(\frac{-p\,|z|}{r}\right)\cos p\psi \qquad (29)$$

for $p\left(|z|-t/2\right)>r\gg|z|+t/2$. In the general case closed integration of (21) over the thickness is not possible

$$B_r^{disc}=\frac{-B_{rem}}{2\pi}\sum_{\bar{\psi}}\int_{\beta=\beta_1}^{\beta_2}\frac{\left(\cos\bar{\psi}\right)\sinh\left(\beta/p\right)\cosh\beta}{\left(\cosh\beta\right)^2-\left(\sin\bar{\psi}\right)^2}d\beta \qquad (30)$$

with $\beta_1=p\,\mathrm{arcsinh}\left(\left(|z|-t/2\right)/r\right)$, $\beta_2=p\,\mathrm{arcsinh}\left(\left(|z|+t/2\right)/r\right)$. For large p one may replace $\sinh\left(\beta/p\right)\to\beta/p$. Then the integral can be solved and leads to a clumsy expression containing poly-logarithms of

---

[‡] For $p=1$ the amplitude $\hat{B}_r^{(no)}$ does not vanish at $r=0$: it has its maximum there and it decreases monotonically versus radial distance.

complex valued arguments. It is more pragmatic to develop $\cosh \beta$ into powers of $\exp(-\beta)$.

$$B_r^{\text{disc}} \cong \frac{B_{rem}}{p\pi} \sum_{\bar{\psi}} \sum_{m=0}^{\infty} (-1)^m \frac{\cos\left((2m+1)\,\bar{\psi}\right)}{2m+1} \exp\left(-\,(2m+1)\,\beta\right)\big|_{\beta_1}^{\beta_2} \quad (31)$$

6.3. The Azimuthal Field Component of Multi-polar Discs

The procedure for the radial component also applies for the azimuthal component. With [33] one gets

$$\lim_{t \to 0} B_\psi^{\text{disc}} = \frac{ptB_{rem}}{2\pi r} \sum_{\bar{\psi}} \frac{\text{Sh}\,(z/r;p)\sin\bar{\psi}}{\cos^2 \bar{\psi} + \text{Sh}^2\,(z/r;p)} \quad (32)$$

The same result is obtained from (19) by use of $\partial B_z/\partial \psi = r\partial B_\psi/\partial z$ (vanishing curl). For finite thickness (32) may be integrated

$$B_\psi^{\text{disc}}(r,\psi,z) = \frac{1}{t} \int_{z'=-t/2}^{t/2} \lim_{t \to 0} B_\psi^{\text{disc}}\left(r,\psi,z-z'\right) dz'. \quad (33)$$

The integration does not seem to be possible in a rigorous analytical way. With (B12) and β_1, β_2 like in (30) it gives

$$B_\psi^{\text{disc}} = \frac{B_{rem}}{2\pi} \sum_{\bar{\psi}} \int_{\beta=\beta_1}^{\beta_2} \frac{\sin\bar{\psi}\cosh\left(\beta/p\right)\sinh\beta}{\left(\sinh\beta\right)^2 + \left(\cos\bar{\psi}\right)^2} d\beta \quad (34)$$

For large p we may approximate $\cosh(\beta/p) \to 1$, which gives

$$B_\psi^{\text{disc}} \cong \frac{-B_{rem}}{2\pi} \sum_{\bar{\psi}} \arctan \frac{\cosh\beta}{\sin\bar{\psi}}\bigg|_{\beta_1}^{\beta_2} \quad (35)$$

(35) and (12) do not fulfill $\partial B_z/\partial \psi = r\partial B_\psi/\partial z$ in a strict sense, because (35) is only an approximation for large p. It is interesting to note that B_ψ is the only field component without overshoot at small air-gaps.

7. THE FIELD OF A STRAIGHT, VERTICALLY MAGNETIZED MULTI-POLAR STRIP

7.1. The Vertical Field Component of Multi-polar Strips

For large reading radius $r \gg \lambda$ one may neglect the curvature of the polarized segments by $r \to \infty$, while the period $\lambda = 2\pi r/p$ remains

constant in (12). This implies $p \to \infty$. In addition, the angular coordinate ψ is replaced by a linear coordinate $x = r\psi$. With (B14) and (B15), (12) reads

$$B_z^{\text{strip}} = \frac{B_{rem}}{2\pi} \left\{ \arctan \left[\frac{2\cos\left(\frac{2\pi x}{\lambda} - \frac{\pi lf}{2}\right) \sinh\left(\frac{\pi t}{\lambda}\right) \cosh\left(\frac{2\pi z}{\lambda}\right)}{\cos^2\left(\frac{2\pi x}{\lambda} - \frac{\pi lf}{2}\right) + \sinh^2\left(\frac{2\pi z}{\lambda}\right) - \sinh^2\left(\frac{\pi t}{\lambda}\right)} \right] + \right.$$
$$\left. \arctan \left[\frac{2\cos\left(\frac{2\pi x}{\lambda} + \frac{\pi lf}{2}\right) \sinh\left(\frac{\pi t}{\lambda}\right) \cosh\left(\frac{2\pi z}{\lambda}\right)}{\cos^2\left(\frac{2\pi x}{\lambda} + \frac{\pi lf}{2}\right) + \sinh^2\left(\frac{2\pi z}{\lambda}\right) - \sinh^2\left(\frac{\pi t}{\lambda}\right)} \right] \right\}. \quad (36)$$

At large air-gaps (36) can be approximated by

$$B_z^{\text{strip}} \cong \frac{4B_{rem}}{\pi} \sinh\left(\frac{\pi t}{\lambda}\right) \cos\left(\frac{\pi lf}{2}\right) \exp\left(\frac{-2\pi |z|}{\lambda}\right) \cos\left(\frac{2\pi x}{\lambda}\right) \quad (37)$$

Note that the vertically polarized strip is assumed to be infinitely wide $w = r_2 - r_1 \to (\infty - 0)$. Hence, the model is a 2D approximation with $\partial/\partial y = 0$ for all field components. Equations (36) and (37) are in agreement with [21].

7.2. The Horizontal Field Component of Multi-Polar Strips

For large radius and large number of pole pairs (32) is

$$\lim_{r \to \infty} \lim_{t \to 0} \vec{n}_\psi \cdot \vec{B}^{\text{disc}} = \frac{t B_{rem}}{\lambda} \sinh\frac{2\pi |z|}{\lambda} \sum_{\bar{\psi}} \frac{\sin\left(\bar{\psi}\right)}{\cosh^2\left(2\pi z/\lambda\right) - \sin^2\left(\bar{\bar{\psi}}\right)} \quad (38)$$

Integration over the thickness gives

$$B_x^{\text{strip}} = \lim_{r \to \infty} \vec{n}_\psi \cdot \vec{B}^{axial\ disc} = \frac{B_{rem}}{4\pi}$$
$$\times \ln \left\{ \frac{\cosh\left(\pi\left(t - 2|z|\right)/\lambda\right) + \sin\left(\pi\left(2x/\lambda - lf/2\right)\right)}{\cosh\left(\pi\left(t - 2|z|\right)/\lambda\right) - \sin\left(\pi\left(2x/\lambda - lf/2\right)\right)} \right.$$
$$\times \frac{\cosh\left(\pi\left(t + 2|z|\right)/\lambda\right) - \sin\left(\pi\left(2x/\lambda - lf/2\right)\right)}{\cosh\left(\pi\left(t + 2|z|\right)/\lambda\right) + \sin\left(\pi\left(2x/\lambda - lf/2\right)\right)}$$
$$\times \frac{\cosh\left(\pi\left(t - 2|z|\right)/\lambda\right) + \sin\left(\pi\left(2x/\lambda + lf/2\right)\right)}{\cosh\left(\pi\left(t - 2|z|\right)/\lambda\right) - \sin\left(\pi\left(2x/\lambda + lf/2\right)\right)}$$
$$\left. \times \frac{\cosh\left(\pi\left(t + 2|z|\right)/\lambda\right) - \sin\left(\pi\left(2x/\lambda + lf/2\right)\right)}{\cosh\left(\pi\left(t + 2|z|\right)/\lambda\right) + \sin\left(\pi\left(2x/\lambda + lf/2\right)\right)} \right\} \quad (39)$$

which is in agreement with [21]. For moderate and large air-gaps (39) may be approximated by

$$B_x^{\text{strip}} \cong \frac{4B_{rem}}{\pi} \sinh\left(\frac{\pi t}{\lambda}\right) \cos\left(lf\frac{\pi}{2}\right) \exp\left(-2\pi\frac{|z|}{\lambda}\right) \sin\left(2\pi\frac{x}{\lambda}\right) \quad (40)$$

For arbitrary air-gap and zero loss factor the amplitude of (39) is given at $x = \lambda/4$ (no overshoot in B_ψ).

$$B_x^{\text{strip}}\left(x = \frac{\lambda}{4}\right) = \frac{B_{rem}}{\pi} \ln \frac{\tanh\left(\pi\left(|z| + t/2\right)/\lambda\right)}{\tanh\left(\pi\left(|z| - t/2\right)/\lambda\right)} \qquad (41)$$

For large $|z|$ (41) goes to (40) while for vanishing air-gap $|z| \to t/2$ the amplitude of the field diverges logarithmically

$$B_x^{\text{strip}}\left(x = \frac{\lambda}{4}, |z| \to \frac{t}{2}\right) = \frac{-B_{rem}}{\pi} \ln\left(\pi \frac{|z| - t/2}{\lambda}\right). \qquad (42)$$

This is in contrast to the z- and r-components, which remain finite even at zero air-gap (cf. (14b) and Fig. 5).

7.3. The Transverse Field Component of Multi-polar Strips

In the limit $r \to \infty$ and $p \to \infty$ with $p/r = 2\pi/\lambda$ the transverse component in (30) vanishes with the order $1/r$.

$$B_y^{\text{strip}} = \frac{-B_{rem}\lambda}{4\pi^2 r} \sum_{\bar\psi} \int_{\beta = 2\pi(|z| - t/2)/\lambda}^{2\pi(|z| + t/2)/\lambda} \frac{\left(\cos\bar\psi\right)\beta\cosh\beta}{\left(\cosh\beta\right)^2 - \left(\sin\bar\psi\right)^2} d\beta \qquad (43)$$

7.4. Comparison of Vertical and Horizontal Components

Since the curl of the B-field vanishes in free space, vertical and horizontal field components are not independent. With (36) and (39) we can prove

$$\partial B_x/\partial z = \partial B_z/\partial x \qquad (44\text{a})$$

The divergence of the field also vanishes in free space. This links the x- and z-components to the y-component:

$$\partial B_y/\partial y = -\partial B_x/\partial x - \partial B_z/\partial z \qquad (44\text{b})$$

With (36) and (39) we get

$$\partial B_y/\partial y = 0 \qquad (44\text{c})$$

Also the higher order derivatives $\partial^n B_y^{\text{strip}}/\partial y^n$ vanish according to (44b). Hence, within the framework of our 2D-model the B_y-field is zero. In reality the B_y-field vanishes only in the center plane $y = 0$ and in fact it is a significant problem for magneto-resistive sensors. Therefore we extend the theory in Sections 9 and 10 to finite widths w of multi-polar strips.
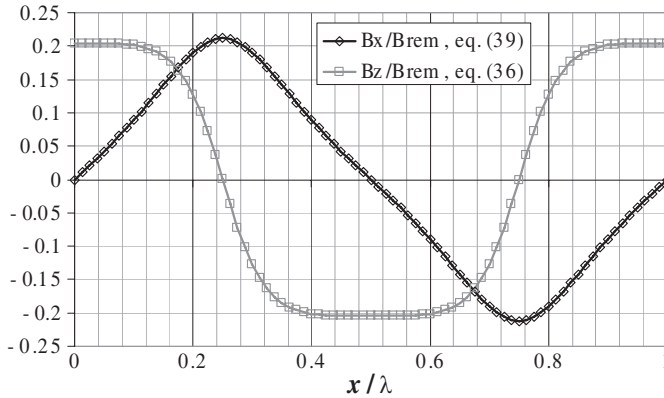
Figure 7. Comparison of vertical and horizontal field components near the limit curve (15a) (i.e., for small yet not very small air-gaps). Both strips are 2 mm thick, each pole extends 6.55 mm ($= \lambda/2$) in x-direction. Test points are 1 mm above the strips. No non-magnetic gap between neighboring north and south poles ($lf = 0$).

All components fade out exponentially at large air-gaps: They drop by a factor of $\exp \pi = 23.1$ if the air-gap increases from λ to 2λ. At large air-gap the amplitudes of both components B_x, B_y are equally strong (as long as $w \to \infty$ still holds).

$$B_z^{\text{strip}} (x = 0, z) = B_x^{\text{strip}} (x = \lambda/4, z) \quad \text{for } z \text{ large.} \quad (45)$$

With the x- and z-components in quadrature and with identical amplitudes this inherently implies the exponential decay versus z: $B_x^{\text{strip}} = f(z) \sin (2\pi x/\lambda)$ and $B_z^{\text{strip}} = f(z) \cos (2\pi x/\lambda)$ in (44a) gives a differential equation with the solution $f(z) \propto \exp (-2\pi z/\lambda)$.

Near the limit curve (15a) (i.e., at small but not very small air-gaps) Fig. 7 shows both field components: B_z is similar to a rectangular waveform whereas B_x resembles a triangular shape. Hence, B_z is steeper at its zero crossings.

At very small air-gaps the horizontal field component has larger spikes than the vertical one due to its poles.

As shown in Fig. 7 the two orthogonal components are in quadrature: B_x assumes extreme values at the zeroes of B_z and vice versa. This may be used in speed sensors [34].

With (37) and (40) one can investigate the effect of a steel-back on the magnetic field of a code wheel in the case of large air-gaps. First we introduce $z = g + t/2$. Due to the method of images one takes

account for the steel back simply by replacing t with $2t$. This leads to

$$\frac{B_x^{\text{strip}} \, (\text{with steel back})}{B_x^{\text{strip}} \, (\text{without steel back})} \cong 1 + \, \exp \frac{-2\pi t}{\lambda} \tag{46}$$

Thus, only for thin code wheels the steel back doubles the magnetic field. For common thicknesses $t/\lambda = 0.2$ the steel back increases the field only by 28%.

8. EFFECTS OF FINITE WIDTH ON THE VERTICAL FIELD COMPONENT OF MULTI-POLAR STRIPS

In Section 6.1 closed-form equations for the axial field component of discs were given. However, in typical code wheel applications the geometry is far from a disc, so that the question arises, in how far the field of a code ring differs from the one of a disc. To this end let us consider a simple geometry with a minimum number of parameters: $r \to \infty$ so that the disc transforms to a linear strip, neglect the loss factor $lf \to 0$ and the thickness of the strip $t \to 0$, and replace the resulting sheet magnetization by a current flowing at its boundaries $M \times t \to I$ as shown in Fig. 8.
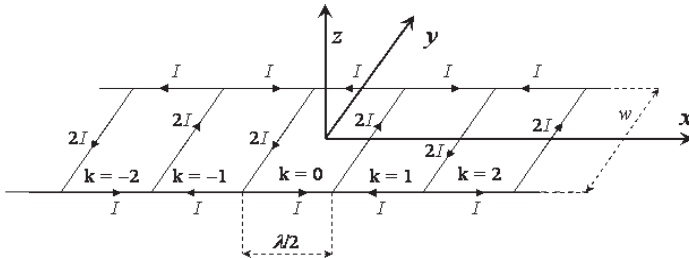

Figure 8. Definition of geometry for a linear strip of finite width w, vanishing loss factor lf and vanishing thickness t. The strip is composed of rectangular sections of length $\lambda/2$ in x-direction and width w in y-direction; within the rectangle the infinitely thin layer is magnetized in positive z-direction for even k and negative z-direction for odd k — k beeing the index of the segment. The magnetization M within each segment can be replaced by a current $I = M \times t$ on its circumference, as shown.

(19) gives the field at $y = 0$ if the width of the strip is infinite

$$B_z^{\text{strip}} \to \frac{2\mu_0 I}{\lambda} \, \frac{\cos\left(\pi\xi\right)\cosh\left(\pi\zeta\right)}{\cos^2\left(\pi\xi\right) + \sinh^2\left(\pi\zeta\right)} \tag{47a}$$
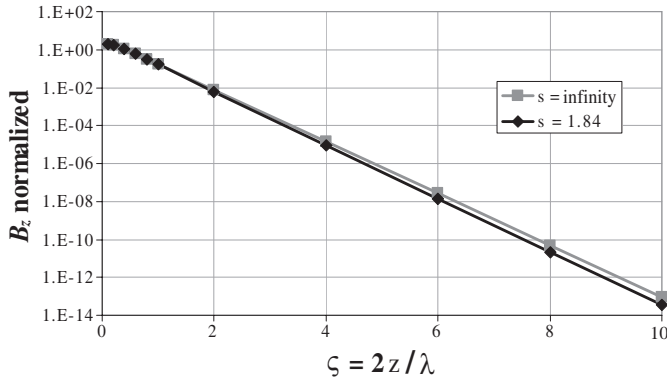
Figure 9. For small width w, i.e., small slimness s, the field decreases slightly steeper than for infinitely wide strips. Yet the difference is negligible for common applications of wheel speed sensing with $\zeta < 3$. $s = 1.84$ is the slimness of a typical code wheel.

with the normalized coordinates $\xi = 2x/\lambda$ and $\zeta = 2z/\lambda$. The primitive interval is spanned by $-1 \leq \xi \leq 1$. On the other hand the law of Biot-Savart gives for the z-component of the field originating from the k-th rectangular current loop

$$B_z^{(k)} = (-1)^k \frac{\mu_0 I}{2\pi\lambda} s \left\{ \frac{0.5-\xi-k}{\sqrt{(0.5-\xi-k)^2+\zeta^2+(s/2)^2}} \left[\frac{1}{(0.5-\xi-k)^2+\zeta^2} + \frac{1}{\zeta^2+(s/2)^2} \right] \right.$$

$$\left. + \frac{0.5+\xi+k}{\sqrt{(0.5+\xi+k)^2+\zeta^2+(s/2)^2}} \left[\frac{1}{(0.5+\xi+k)^2+\zeta^2} + \frac{1}{\zeta^2+(s/2)^2} \right] \right\} \quad (47b)$$

with the slimness of the strip $s = 2w/\lambda$. The total field is obtained by a summation over all k: $-\infty \leq k \leq \infty$. Fig. 9 compares the amplitude of the vertical field B_z versus air-gap for $s = \infty$ and $s = 1.84$ (which is the slimness of a typical encoder ring JT65, cf. Fig. 6). The difference is small at small air gaps. At larger air gaps the narrow strip has smaller field than the infinitely wide strip: at $\zeta = 1$ the difference is 5%, at $\zeta = 2$ it is 20%, and at $\zeta = 10$ it is 60%.

9. THE TRANSVERSE FIELD OF MULTI-POLAR STRIPS

In Sections 7.3 and 7.4 we saw that our two-dimensional model is not able to describe the magnetic field component parallel to the width of the multi-polar strip. Nevertheless, for magneto-resistive sensors this

component is of considerable interest. So we derive it from the vector potential of a magnetic dipole [35]:

$$d^3 \vec{A}_p = \frac{B_{rem}(\vec{r'})}{4\pi} \vec{n}_z \times \frac{\vec{r} - \vec{r'}}{|\vec{r} - \vec{r'}|^3} dx' dy' dz' \qquad (48)$$

With $\vec{B} = \vec{\nabla} \times \vec{A}_p$ we get

$$d^3 B_y(\vec{r}) = \frac{3 B_{rem}(\vec{r'})}{4\pi} \frac{(y - y')(z - z') dx' dy' dz'}{\left((x - x')^2 + (y - y')^2 + (z - z')^2\right)^{5/2}} \qquad (49)$$

Integration over $-w/2 < y' < w/2$ and $-t/2 < z' < t/2$ is simple since $B_{rem}(\vec{r'})$ is only a function of x'. We develop the periodic magnetization pattern into a Fourier series

$$B_{rem}(\vec{r'}) = \sum_{n=0}^{\infty} (-1)^n \frac{4 B_{rem}}{\pi(2n+1)} \cos\left(\pi\left(n + \frac{1}{2}\right) lf\right) \cos\left(2\pi(2n+1)\frac{x'}{\lambda}\right) \qquad (50)$$

The final integration over $-\infty < x' < \infty$ gives

$$B_y = \frac{2 B_{rem}}{\pi^2} \sum_{n=0}^{\infty} \frac{(-1)^n}{2n+1} \cos\left(\pi\left(n + \frac{1}{2}\right) lf\right) \cos\left(2\pi(2n+1)\frac{x}{\lambda}\right)$$

$$\times K_0\left(\frac{\pi}{\lambda}(2n+1)\sqrt{\eta^2 + \zeta^2}\right) \Bigg|_{\eta = 2y - w}^{|2y+w} \Bigg|_{\zeta = 2z - t}^{|2z+t} \qquad (51)$$

with the modified Bessel function K_0. A closed form summation over index n seems not to be possible, but luckily K_0 falls off drastically for large arguments. If we use only the lowest order term $n = 0$ the error is less than 1% for $\sqrt{(2|y| - w)^2 + (2|z| - t)^2}\Big/\lambda > 0.66$ and it is less than 0.1% for $\sqrt{(2|y| - w)^2 + (2|z| - t)^2}\Big/\lambda > 1.02$. Therefore the solution (51) with $n = 0$ is a good approximation for test points not too close to the edges $y = \pm w/2$, $z = \pm t/2$ of the strip (cf. Fig. 10).

For small y we may expand (51) into a Taylor series in y and for large $\sqrt{w^2 + (2|z| - t)^2}\Big/\lambda$ we may use the asymptotic expansion for the Bessel functions [36], which gives

$$B_y \approx \frac{8 B_{rem}}{\pi} \frac{wy}{\sqrt{2\lambda}} \cos\left(\frac{\pi}{2} lf\right) \cos\left(2\pi\frac{x}{\lambda}\right)$$

$$\times \left\{ \frac{\exp\left(-\frac{\pi}{\lambda}\sqrt{w^2 + (2z - t)^2}\right)}{\left(w^2 + (2z - t)^2\right)^{3/4}} - \frac{\exp\left(-\frac{\pi}{\lambda}\sqrt{w^2 + (2z + t)^2}\right)}{\left(w^2 + (2z + t)^2\right)^{3/4}} \right\} \qquad (52a)$$

For most sensor applications one of the two terms in (52a) dominates so that we obtain a short approximation for small y

$$
B_y \approx \frac{8B_{rem}}{\pi} \frac{wy \mathrm{sgn}\,(z)}{\sqrt{2\lambda}} \cos\left(\frac{\pi}{2} lf\right) \cos\left(2\pi \frac{x}{\lambda}\right) \left(w^2 + (2\,|z| - t)^2\right)^{-3/4}
$$
$$
\times \exp\left(-\frac{\pi}{\lambda}\sqrt{w^2 + (2\,|z| - t)^2}\right) \tag{52b}
$$

For y close $\pm w/2$ to and z close to $\pm t/2$ there is again a single dominant term in (51) which gives

$$
B_y \approx \frac{2B_{rem}}{\pi^2} \sum_{n=0}^{\infty} (-1)^n \frac{\mathrm{sgn}\,(yz)}{2n+1} \cos\left(\pi\left(n+\frac{1}{2}\right) lf\right) \cos\left(2\pi(2n+1)\frac{x}{\lambda}\right)
$$
$$
\times K_0\left(\frac{\pi}{\lambda}(2n+1)\sqrt{(2\,|y|-w)^2 + (2\,|z|-t)^2}\right) \tag{53a}
$$

Near the edges of the strip the field diverges logarithmically

$$
\lim_{2|y|\to w \,\wedge\, 2|z|\to t} B_y = \frac{-B_{rem}}{\pi^2} \mathrm{sgn}\,(yz) \cos\left(\frac{\pi}{2} lf\right)
$$
$$
\times \cos\left(2\pi\frac{x}{\lambda}\right) \ln\left(\left(\frac{2\,|y|-w}{\lambda}\right)^2 + \left(\frac{2\,|z|-t}{\lambda}\right)^2\right) \tag{53b}
$$

For test points not too close to the edges of the multi-polar strip we may again use the asymptotic expansion for the Bessel functions for large arguments to get

$$
B_y \approx \mathrm{sgn}\,(yz)\sqrt{2\lambda}\frac{B_{rem}}{\pi^2} \cos\left(\frac{\pi}{2} lf\right) \cos\left(2\pi\frac{x}{\lambda}\right) \frac{\exp\left(\frac{-\pi}{\lambda}\sqrt{(2\,|y|-w)^2 + (2\,|z|-t)^2}\right)}{\left((2\,|y|-w)^2 + (2\,|z|-t)^2\right)^{1/4}} \tag{54}
$$

The B_y-field is in phase with the B_z-field and in quadrature to the B_x-field. Therefore the projection of the B-vector into the xy-plane rotates on an ellipse with long axis in x and short axis in y directions. The B_y-field is zero in the symmetry plane $y = 0$. It increases linearly in y for small y, and it decreases exponentially for large widths of the multi-polar strip. Therefore it is good practice to use wide strips ($w = 12\ldots 15\,\mathrm{mm}$) for magneto-resistive sensors.

Since the curl of the magnetic field vanishes in free space we get $\partial B_x/\partial y = \partial B_y/\partial x$ and $\partial B_z/\partial y = \partial B_y/\partial z$. Therefore we obtain the

y-dependence of B_x- and B_z-fields by integration

$$B_x\left(x,y,z\right) = -\int\limits_{y'=y}^{\infty} \frac{\partial B_y\left(x,y',z\right)}{\partial x}dy', \tag{55a}$$

$$B_z\left(x,y,z\right) = -\int\limits_{y'=y}^{\infty} \frac{\partial B_y\left(x,y',z\right)}{\partial z}dy' \tag{55b}$$

Inserting (51) into (55a) and (55b) gives accurate 3D-formulae for the fields of pole-strips with finite width w. A Taylor series expansion for small y shows that the B_x- and B_z-fields depend parabolically on y yet only the B_z- component may have a vanishing curvature:

$$\left.\frac{\partial^2 B_x}{\partial y^2}\right|_{y=0} = \left.\frac{\partial^2 B_y}{\partial x \partial y}\right|_{y=0}$$

$$= 16 B_{rem}\frac{w}{\lambda^2}\sum_{n=0}^{\infty}(-1)^n(2n+1)\cos\left(\pi\left(n+\frac{1}{2}\right)lf\right)$$

$$\times \sin\left(2\pi(2n+1)\frac{x}{\lambda}\right)K_1\left(\frac{\pi}{\lambda}(2n+1)\sqrt{w^2+\zeta^2}\right)\Bigg/\sqrt{w^2+\zeta^2}\Bigg|_{\zeta=2z-t}^{2z+t} \tag{56a}$$
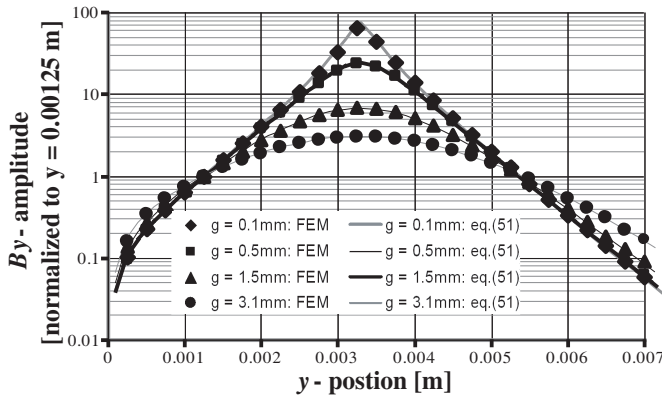

Figure 10. B_y-field of a multipolar strip: Comparison of analytical solution (51) ($n = 0$ term only) with finite-element simulations (FEM) shows good agreement for all air-gaps g and all y-positions even beyond the edge of the strip. Strip data: remanence $= 500\,\text{mT}$, coercivity Hcb $= 355\,\text{kA/m}$, $\lambda = 4\,\text{mm}$, $w = 6.6\,\text{mm}$, $t = 2.4\,\text{mm}$, with steelback. The maximum B_y-field is given at the edge of the strip $y = w/2$.

This curvature is always negative — there is no real zero for it.

$$\frac{\partial^2 B_z}{\partial y^2}\bigg|_{y=0} = \frac{\partial^2 B_y}{\partial y \partial z}\bigg|_{y=0}$$

$$= 16 B_{rem}\frac{w}{\lambda^2}\sum_{n=0}^{\infty}(-1)^n(2n+1)\cos\left(\pi\left(n+\frac{1}{2}\right)lf\right)$$

$$\times \cos\left(2\pi(2n+1)\frac{x}{\lambda}\right)\zeta K_2\left(\frac{\pi}{\lambda}(2n+1)\sqrt{w^2+\zeta^2}\right)\Big/\left(w^2+\zeta^2\right)\bigg|_{\zeta=2z-t}^{2z+t} \quad (56b)$$

In the $n = 0$-approximation this function has a zero: e.g., for $z = 3.0\,\text{mm}$, $w = 14\,\text{mm}$, $t = 2\,\text{mm}$, and $\lambda = 11.78\,\text{mm}$. Therefore sensor systems which detect the B_z-component can be made more robust against position tolerances. This is an advantage of Hall plates over magneto-resistors in true power-on sensors.

Inserting (51) into (55a) and (55b) and developing for $t^2 + w^2 \ll y^2 + z^2$ gives the three-dimensional fields at large distance,

$$\begin{rcases} B_x \\ B_y \\ B_z \end{rcases} \cong \frac{B_{rem}tw}{\pi\lambda^{3/2}}\cos\left(\frac{\pi}{2}lf\right)\frac{\exp\left(-\frac{2\pi}{\lambda}\sqrt{y^2+z^2}\right)}{(y^2+z^2)^{5/4}}$$

$$\begin{cases} z\left[\lambda + 4\pi\sqrt{y^2+z^2}\right]\sin(2\pi x/\lambda) \\ yz\left[4\pi + \frac{4\lambda}{\sqrt{y^2+z^2}} + \frac{5\lambda^2}{4\pi(y^2+z^2)}\right]\cos\left(2\pi\frac{x}{\lambda}\right) \quad (57) \\ \left[\lambda(z^2-2y^2)\Big/\sqrt{y^2+z^2} + 4\pi z^2\right]\cos(2\pi x/\lambda) \end{cases}$$

For $|y| \ll |z|$ one gets a simple far-field approximation

$$\begin{rcases} B_x \\ B_y \\ B_z \end{rcases} \cong \frac{4B_{rem}tw}{\lambda^{3/2}\sqrt{|z|}}\cos\left(\frac{\pi}{2}lf\right)\exp\left(\frac{-2\pi|z|}{\lambda}\right)\begin{cases} \sin(2\pi x/\lambda) \\ (y/z)\cos(2\pi x/\lambda) \quad (58) \\ \cos(2\pi x/\lambda) \end{cases}$$

So the 3D-fields of (58) decrease by an extra factor $w\big/\sqrt{\lambda z}$ in contrast to (37). With the data of Fig. 9 this gives 0.41 for $\zeta = 10$, which agrees well with the reported -60%.

10. TORQUES BETWEEN MULTI-POLAR DISCS

Torques transmitted in permanent magnetic couplings are subject of recent research [37–42]. The force density of a magnetic field onto some magnetization pointing in z-direction is $\vec{f} = M\vec{\nabla}B_z$. In the case of discs or rings we are interested in the tangential component of the

nabla operator: $(1/r) \, \partial/\partial\psi$. The torque is obtained by integration of radial distance times force density over the volume of the ring

$$T = \int r f_\psi dV = 2p \frac{B_{rem}}{\mu_0} \int\limits_{r=r_1}^{r_2} \int\limits_{\psi=\psi_0-\pi(1-lf)/(2p)}^{\psi_0+\pi(1-lf)/(2p)} \int\limits_{z=g+t/2}^{g+3t/2} r \frac{1}{r} \frac{\partial B_z}{\partial \psi} r dr d\psi dz$$

$$= \frac{2pB_{rem}}{\mu_0} \int\limits_{r=r_1}^{r_2} \int\limits_{z=g+t/2}^{g+3t/2} B_z\left(r, \bar\psi, z\right) r dr dz \Big|_{\bar\psi=\psi_0-\pi(1-lf)/(2p)}^{\psi_0+\pi(1-lf)/(2p)} \tag{59}$$

where ψ_0 specifies the angular shift between both pole rings. We assume that they have identical shape and rotation axis. In axial direction they are a distance g apart. For the sake of convenience they are supposed to have no steel-back. B_r and B_z are related due to the fact that the curl vanishes

$$B_z\left(r, \bar\psi, z\right) = \int\limits_{\bar r=0}^{r} \frac{\partial B_r\left(\bar r, \bar\psi, z\right)}{\partial z} d\bar r \tag{60}$$

(60) does not need an additive constant because B_z vanishes at $r = 0$ due to (13). Inserting (60) into (59) with $lf = 0$ gives

$$T = \frac{2pB_{rem}}{\mu_0} \int\limits_{r'=r_1}^{r_2} \int\limits_{\bar r=0}^{r'} r' B_r\left(\bar r, \bar\psi, \bar z\right) d\bar r dr' \Big|_{\bar\psi=\psi_0-\pi/(2p)}^{\psi_0+\pi/(2p)} \Big|_{\bar z=g+t/2}^{g+3t/2} \tag{61}$$

Let r_1 go to zero. Reversing the sequence of integration and carrying out the inner integral gives

$$T = \frac{2pB_{rem}}{\mu_0} \int\limits_{\bar r=0}^{r_2} \left(r_2^2 - \bar r^2\right) B_r\left(\bar r, \psi_0 + \pi/(2p), \bar z\right) d\bar r \Big|_{\bar z=g+t/2}^{g+3t/2} \tag{62}$$

In the following we use (62) to derive a criterion for maximum torque in the limit of thin discs. From (62) we get

$$\lim_{t\to 0} T = \frac{2ptB_{rem}}{\mu_0} \int\limits_{r=0}^{r_2} \left(r_2^2 - r^2\right) \frac{\partial \lim\limits_{t\to 0} B_r\left(r, \psi_0 + \pi/(2p), g\right)}{\partial z} dr \tag{63}$$

Replacing $\partial B_r/\partial z = \partial B_z/\partial r$ in the first term of the integrand that is multiplied by r_2^2 and using (22) for the term that is multiplied by r^2 gives

$$\lim_{t\to 0} T = 2pt \frac{B_{rem}}{\mu_0} \left\{ r_2^2 \lim_{t\to 0} B_z\left(r, \psi_0 + \frac{\pi}{2p}, g\right) \Big|_{r=0}^{r_2} + \frac{\partial}{\partial z} z \int\limits_{r=0}^{r_2} r \lim_{t\to 0} B_z\left(r, \psi_0 + \frac{\pi}{2p}, z\right) dr \Big|_{z=g} \right\} \tag{64}$$

With (19) we get

$$\lim_{t \to 0} B_z \left(r, \psi_0 + \frac{\pi}{2p}, z \right) = \frac{-ptB_{rem}}{\pi\sqrt{r^2 + z^2}} \frac{\sin\left(p\psi_0\right)\cosh\left(p\operatorname{arcsinh}\left(z/r\right)\right)}{\left[\sinh\left(p\operatorname{arcsinh}\left(z/r\right)\right)\right]^2 + \left[\sin\left(p\,\psi_0\right)\right]^2} \quad (65)$$

If we ignore overshoot the maximum torque is at $p\psi_0 = \pi/2$. There the integral in (64) can be transformed into

$$-zt\frac{B_{rem}}{\pi} \int\limits_{\beta = \operatorname{parcsinh}(z/r_2)}^{\infty} \frac{1}{(\sinh(\beta/p))^2} \frac{d\beta}{\cosh\beta} \quad (66)$$

An exact analytical solution of (66) seems not possible. Yet, if we replace $\sinh\left(\beta/p\right) \to \beta/p$ we get a good approximation: numerical investigation shows that the error is largest for large $p\operatorname{arcsinh}\left(z/r_2\right)$ and small p. For $p\operatorname{arcsinh}\left(z/r_2\right) < 2$ and $p \geq 5$ the error is less than 10%, for $p \geq 9$ less than 3.3%, and for $p \geq 16$ less than 1%. With

$$1/\cosh\beta \cong 2\left(\exp\left(-\beta\right) - \exp\left(-3\beta\right) + \exp\left(-5\beta\right) \mp \ldots\right) \quad (67)$$

the integral of (66) can be developed into a series

$$\frac{2p^2 ztB_{rem}}{\pi} \sum_{m=0}^{\infty} (-1)^{m+1} \left\{ \frac{\exp\left[-(2m+1)p\operatorname{arcsinh}(z/r_2)\right]}{p\operatorname{arcsinh}(z/r_2)} \right.$$

$$\left. -(2m+1)\Gamma\left(0, (2m+1)p\operatorname{arcsinh}\frac{z}{r_2}\right) \right\} \quad (68)$$

$\Gamma\left(a, x\right) = \int_x^{\infty} t^{a-1}\exp\left(-t\right)dt$ is the upper incomplete gamma function. Inserting this into (64) and skipping terms that vanish at large p gives

$$\lim_{t \to 0} \hat{T}^{(no)} \cong \frac{(2B_{rem}pt)^2}{\mu_0\pi} \left\{ \frac{r_2}{\cosh(pg/r_2)} - 2pg\sum_{m=0}^{\infty}(-1)^m(2m+1)\Gamma\left(0, (2m+1)\frac{pg}{r_2}\right) \right\} \quad (69)$$

The index $\hat{T}^{(no)}$ reminds us that we considered the non-overshoot regime only. (69) agrees up to 0.5% with a finite element simulation for $p = 10$, $t = 5\,\text{mm}$, $g = 5\,\text{mm}$, $r_2 = 150\,\text{mm}$ (where we used an effective air-gap $g_{eff} = g + t$ in (69)). The torque amplitude $\hat{T}^{(no)}$ increases versus r_2 and it decreases versus g, yet it is non-monotonic versus p. Differentiating (69) against p and equating for zero gives an equation for the *single* parameter pg/r_2 that can be solved numerically: the optimum number of poles for maximum torque transmission is

$$p\,g/r_2 \cong 1.51812 \quad (70)$$

For $r < r_2$ this implies $pz/r > 1.51812$ so that during the integration of (64) the B_z-field has no overshoot, because overshoot occurs only

at $pz/r < \mathrm{arcsinh}\,(1) = 0.8814$. It means that the optimum disc has such a small diameter that even at its perimeter no overshoot of the B_z-field occurs.

Inserting (70) into (69) gives the maximum obtainable torque

$$\lim_{t \to 0} \hat{T}^{(\mathrm{no})}_{\max} \cong 0.409028 \times \frac{B^2_{rem} t^2 r^3_2}{\mu_0 g^2} \qquad (71)$$

It goes up with the cube of the diameter and the square of the thickness and down with the square of the gap.

Our reflections assumed a field generating disc with $r_2 \to \infty$, so that we ignored the effects of equivalent sheet currents in azimuthal direction (4b). They have only negligible effect on the torque, because they alter the B_r-field only close to $r = r_2$. According to (62) the B_r-field is multiplied by $r^2_2 - \bar{r}^2$ before integration, and this strongly dampens the error near $\bar{r} = r_2$. Therefore our theory applies to discs with $z \ll r_2$, yet not to slim rings with $r_2 - r_1$ in the order of z.

In the foregoing we focused on large p so that we still need to consider what happens at small p. It is straightforward to set $p = 1, 2, 3, \ldots$ in (66) and perform the integration in closed form (for $p < 7$) or numerically. Fig. 11 compares these results with (69): The $p = 1$ curve is different from all others: it has no relative extremum. For $p > 5$ the curves are nearly identical.

Figure 11 shows that for small pg/r_2 the torque rises whereas for large pg/r_2 the torque decreases. This was found experimentally and numerically in [43–46] — here we have proven it analytically.

So far we have excluded overshoot in the B_z-field. This is admissible for $pz/r_2 > \mathrm{arcsinh}\,(1) \cong 0.8814$ but for smaller values could there be a torque larger than that given by (71)? Given the size of the discs and the gap between them what is the optimum number of pole pairs? With $p \cong 1.51812 \times r_2/g$ the torque is maximum in the non-overshoot regime of B_z. Reducing p down to $p \cong 0.8814 \times r_2/z$ there is still no overshoot of B_z and so the torque reduces (by 21.4% according to (69)). Further reduction of p reduces the torque at $\psi_0 = \pi/(2p)$, but starts to add torque left and right of this angle ψ_0. Thus, even though B_z exhibits overshoot, the torque does not yet show overshoot. Since B_z- and B_r-overshoot is strongest at the perimeter of the disc it is damped much by the factor $r^2_2 - \bar{r}^2$ in (62). Only at very small p a significant portion of the disc exhibits B_z-overshoot and this finally leads to an overshoot in the torque function $T(\psi_0)$. It can be found by solving $\partial^2 T / \partial \psi^2_0 = 0$ at $\psi_0 = \pi/(2p)$. This can be done in a rigorous way (i.e., for arbitrary g/r_2 and p) by differentiating (64) twice against

ψ_0. One ends up with an implicit equation for g/r_2 as a function of p:

$$\int_{\beta=p\arcsinh(g/r_2)}^{\infty} \left(1 - \frac{2}{(\cosh\beta)^2}\right) \frac{d\beta}{[\sinh(\beta/p)]^2 \cosh\beta} = 0 \qquad (72)$$

The result is $pg/r_2 = 0.6601$ for $p = 1$, $pg/r_2 = 0.5853$ for $p = 2$, ... and 0.5555 for large p. This gives a limit curve for the torque: for larger pg/r_2 the torque has no overshoot, for smaller pg/r_2 the torque exhibits overshoot. So, although the B_z-field shows an overshoot at $pz/r_2 \cong 0.8814$ it still takes much lower $pg/r_2 \leq 0.5555$ for overshoot in the torque. A look at Fig. 11 shows that at such low p-values the torque is only about half of its maximum at $pg/r_2 \cong 1.51812$. For the following it is important to be aware that (69) gives the correct torque amplitude for $pg/r_2 \geq 0.5555$. With this in mind we can prove rigorously that even in the regime of torque overshoot (i.e., for $pg/r_2 < 0.5555$) this overshoot cannot exceed the value of (71), which is therefore the global maximum.
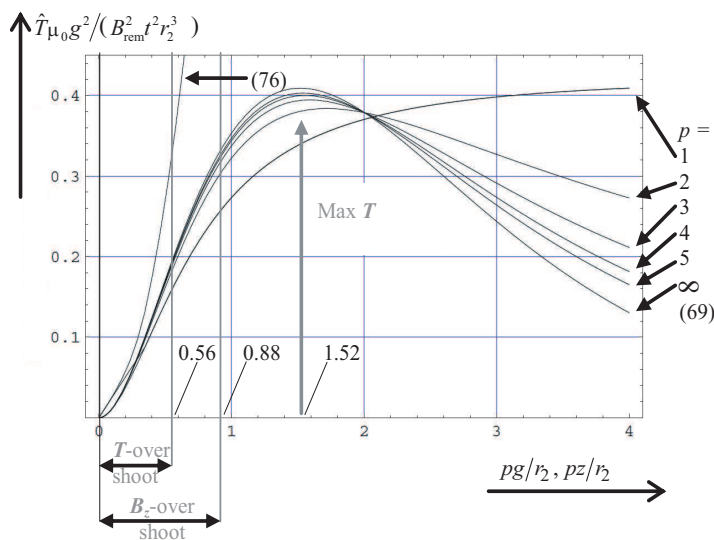

Figure 11. Normalized torque amplitudes for thin discs $t \to 0$. Comparison of solution (69) for large p with specific solutions for $p = 1, 2, \ldots 5$. The maximum torque is given at $pg/r_2 = 1.52$. The region of overshoot in B_z ($pz/r_2 < 0.88$) is larger than the region of overshoot in torque ($pg/r_2 < 0.56$). Torque amplitudes are below the line labeled with Equation (76).

So we have to prove the following hypothesis

$$0.409028 > \frac{\mu_0 g^2}{B_{rem}^2 t^2 r_2^3} \lim_{t\to 0} |T| \quad \text{for} \quad 0 < pg/r_2 < 0.5555 \qquad (73)$$

Inserting (19) into (59) gives an integral that cannot be solved in closed form. So we manipulate it in such a way, that its values increases and that we can solve it. If we can finally show that even this increased value satisfies (73), the proof is complete. With $g/r = \sinh\beta$ and $|\sin(p\psi_0)| = \sigma$ we get

$$\frac{\mu_0 g^2}{B_{rem}^2 t^2 r_2^3} \lim_{t\to 0} |T| = \frac{4}{\pi}\left(\frac{pg}{r_2}\right)^3 \int\limits_{\beta=pg/r_2}^{\infty} \frac{1}{(p\sinh(\beta/p))^2} \frac{\sigma\cosh\beta}{\sigma^2+(\sinh\beta)^2} \, d\beta \quad (74)$$

This integral may be split in two parts. The first part is for small β, where we use $p\sinh(\beta/p) > \beta$ and the hyperbolic functions are bound by polynomials,

$$\int\limits_{\beta=pg/r_2}^{\text{arcsinh}(1)} \frac{1}{(p\sinh(\beta/p))^2} \frac{\sigma\cosh\beta}{\sigma^2+(\sinh\beta)^2} \, d\beta < \int\limits_{\beta=pg/r_2}^{\text{arcsinh1}} \frac{\sigma}{\beta^2} \frac{1+2133\beta^2/4000}{\sigma^2+(1135\beta/1000)^2} \, d\beta \, (75a)$$

The integration gives a lengthy expression. The second part of the integral in (74) is for $\beta > \text{arcsinh}(1)$, which is equivalent to $p\sinh(\beta/p) > \text{arcsinh}(1)$. The integrand may be expanded into powers of $\exp(-\beta)$ like in (67) and integrated term by term. The resulting infinite sum is found to be identical to the arctan-function.

$$\int\limits_{\beta=\text{arcsinh}(1)}^{\infty} \frac{1}{(p\sinh(\beta/p))^2} \frac{\sigma\cosh\beta}{\sigma^2+(\sinh\beta)^2} d\beta < \frac{\arctan\sigma}{(\text{arcsinh1})^2} \qquad (75b)$$

Inserting (75a) and (75b) into (74) gives an upper limit for the torque

$$\lim_{t\to 0} |T| \frac{\mu_0 g^2}{B_{rem}^2 t^2 r_2^3} < \frac{4}{\pi}\left(\frac{pg}{r_2}\right)^3 \left\{ \frac{\arctan\sigma}{(\text{arcsinh1})^2} - \frac{1/\text{arcsinh1}}{\sigma} + \frac{r_2}{pg\sigma} \right.$$
$$\left. + \left(\frac{2133}{4540} - \frac{227}{200\sigma^2}\right)\left(\arctan\frac{227\text{arcsinh1}}{200\sigma} - \arctan\frac{227pg}{200\sigma r_2}\right) \right\} \qquad (76)$$

The right hand side of (76) is largest at $\sigma = |\sin(p\psi_0)| = 1$. There it is a monotonic function of pg/r_2 and attains a value of 0.409028 for $pg/r_2 = 0.61409$. In the required range $0 < pg/r_2 < 0.5555$ it assumes values between 0 and 0.3336 and therefore (73) holds, q.e.d.. This is also shown in Fig. 11.

11. CONCLUSION

The magnetic field of axially magnetized multi-pole rings was calculated analytically for single poles. In the limit of vanishing inner and infinite outer diameter the ring degenerates to a disc. This simplified model offers the advantage to describe the magnetic field without elliptic integrals. This allows us to calculate the axial component in closed form by summing up the contributions of all poles. The resulting formulae are a good approximation to the field of real encoders, as is proven by measurement (Fig. 6) and calculation (Fig. 9). Equation (12) can be used to describe code-wheels with high number of alternating poles as well as magnetic gears and permanent magnet motors with only a few, large alternating poles.

In the limit of large reading radius the disc degenerates to a linear strip of infinite width. Both vertical and horizontal field components of this 2D-model were given in closed form by (28a) and (29b). For small air-gaps the vertical field is pulse shaped while the horizontal field has a triangular waveform. For moderate and large air-gap the field is sinusoidal. This is described by (28b) and (29c) with amplitudes decaying exponentially versus air-gap. Vertical and horizontal field components are phase shifted by 90 degrees and their amplitudes are identical (34). With higher pole count the field increases at the surface of the encoder while it falls off more drastically versus air-gap. The transverse field component B_y is the key to derive the other field components in a strict 3D-theory (Section 9). This theory is applied to optimize pole-strips in such a way that the vertical field component B_z has a flat plateau versus transverse position y (50). With these equations it is possible to study the influence of assembly tolerances on wheel speed sensors.

The transmitted torque of axially magnetized couplings is maximized by avoiding overshoot in the fields and in the torque function. The optimum number of pole-pairs is 1.5 times the radius of the discs divided by the gap between both discs (70). This holds also for arbitrarily thick discs as will be shown in a follow-up paper.

APPENDIX A.

Here is a derivation of (11) because it is not given in tables on finite sums (like e.g., [47]). Let $\zeta = i \sin \alpha$, α a complex number and i the imaginary unit, then the LHS of (11) reads

$$\sum_{k=0}^{2p-1} (-1)^k \left\{ \arctan \frac{i \sin \alpha}{\sin (y - \pi k/p)} + \arctan \frac{i \sin \alpha \cot (y - \pi k/p)}{\cos \alpha} \right\}. \text{(A1)}$$

With the identity $\arctan iz = 1/(2i) \ln[(1-z)/(1+z)]$ one gets

$$\frac{1}{2i}\sum_{k=0}^{2p-1}(-1)^k\ln\left\{\frac{\sin(y-\pi k/p)-\sin\alpha}{\sin(y-\pi k/p)+\sin\alpha}\times\frac{\cos\alpha\sin(y-\pi k/p)-\sin\alpha\cos(y-\pi k/p)}{\cos\alpha\sin(y-\pi k/p)+\sin\alpha\cos(y-\pi k/p)}\right\},\quad\text{(A2)}$$

which — by use of the addition theorems for sine and cosine functions — can be rewritten as

$$\sum_{k=0}^{2p-1}\frac{(-1)^k}{2i}\ln\left(\frac{\sin\left((y-\alpha-\pi k/p)/2\right)\cos\left((y+\alpha-\pi k/p)/2\right)}{\sin\left((y+\alpha-\pi k/p)/2\right)\cos\left((y-\alpha-\pi k/p)/2\right)}\right.$$
$$\left.\times\frac{\sin\left((y-\alpha-\pi k/p)/2\right)\cos\left((y-\alpha-\pi k/p)/2\right)}{\sin\left((y+\alpha-\pi k/p)/2\right)\cos\left((y+\alpha-\pi k/p)\right)}\right)\quad\text{(A3)}$$

Canceling common terms in nominator and denominator gives

$$2\frac{1}{2i}\sum_{k=0}^{2p-1}(-1)^k\ln\frac{\sin\left((y-\alpha-\pi k/p)/2\right)}{\sin\left((y+\alpha-\pi k/p)/2\right)}.\quad\text{(A4)}$$

This sum can be split up into two parts, one containing only even indices $k = 2l$ with $0 \le l \le p-1$ and the other only odd indices $k = 2l+1$ with $0 \le l \le p-1$.

$$\frac{1}{i}\ln\left\{\frac{\prod_{k=0}^{p-1}\sin\left(\frac{\alpha-y}{2}+\pi k/p\right)\sin\left(-\frac{y+\alpha-\pi/p}{2}+\pi k/p\right)}{\prod_{k=0}^{p-1}\sin\left(-\frac{y+\alpha}{2}+\pi k/p\right)\sin\left(\frac{\alpha-y+\pi/p}{2}+\pi k/p\right)}\right\}\quad\text{(A5)}$$

By use of the identity $\sin px = 2^{p-1}\prod_{k=0}^{p-1}\sin\left(x+\pi k/p\right)$ given in [48] (A5) transforms to

$$2\frac{1}{2i}\ln\left\{\frac{\sin\left((y-\alpha)\,p/2\right)}{\sin\left((y+\alpha)\,p/2\right)}\times\frac{\cos\left((y+\alpha)\,p/2\right)}{\cos\left((y-\alpha)\,p/2\right)}\right\}\quad\text{(A6)}$$

which can be rewritten as inverse tangent

$$= 2\arctan\left\{i\sin\left(p\alpha\right)/\sin\left(py\right)\right\},\quad\text{(A7)}$$

The argument can be manipulated as

$$i\sin\left(p\alpha\right) = i\sin(p\arcsin\left(-i\zeta\right) = i\sin\left(pi\ln\left(\sqrt{1+\zeta^2}-\zeta\right)\right)$$
$$= i\sin\left(i\ln\left(\sqrt{1+\zeta^2}-\zeta\right)^p\right)=i^2\sinh\ln\left(\sqrt{1+\zeta^2}-\zeta\right)^p$$
$$= \left[\left(\zeta+\sqrt{1+\zeta^2}\right)^p-\left(\zeta+\sqrt{1+\zeta^2}\right)^{-p}\right]\Big/2=\text{Sh}\left(\zeta;p\right)\quad\text{(A8)}$$

which finally renders the result at the RHS of (11). From this equation many similar ones can be derived by substitution or differentiation.

APPENDIX B.

We define the functions

$$\mathrm{Sh}\,(\zeta;p) = \left(\omega^p - \omega^{-p}\right)/2 \quad \text{and} \quad \mathrm{Ch}\,(\zeta;p) = \left(\omega^p + \omega^{-p}\right)/2 \quad \text{(B1)}$$

with $\omega = \zeta + \sqrt{1 + \zeta^2}$, ζ and p being real numbers. Since $\omega > 0$ it is clear that $\mathrm{Ch}\,(\zeta;p) > 0$ holds. $\mathrm{Sh}\,(\zeta;p) = -\mathrm{Sh}\,(-\zeta;p)$ is an odd function. Hence $\mathrm{Sh}\,(0;p) = 0$. $\mathrm{Ch}\,(\zeta;p) = \mathrm{Ch}\,(-\zeta;p)$ is an even function with $\mathrm{Ch}\,(0;p) = 1$. The first derivatives are

$$\frac{\partial\,\mathrm{Sh}\,(\zeta;p)}{\partial\zeta} = \frac{p\,\mathrm{Ch}\,(\zeta;p)}{\sqrt{1+\zeta^2}}, \quad \text{(B2)}$$

$$\frac{\partial\,\mathrm{Ch}\,(\zeta;p)}{\partial\zeta} = \frac{p\,\mathrm{Sh}\,(\zeta;p)}{\sqrt{1+\zeta^2}} \quad \text{(B3)}$$

The first derivative of $\mathrm{Sh}\,(\zeta;p)$ is positive — therefore $\mathrm{Sh}\,(\zeta;p)$ is strictly monotonically rising. Analogously $\mathrm{Ch}\,(\zeta;p)$ is monotonic for $\zeta \geq 0$. MacLaurin expansions are

$$\mathrm{Sh}(\zeta;p) \cong p\,\zeta + p\left(p^2 - 1\right)\zeta^3/6 \quad \text{and} \quad \mathrm{Ch}(\zeta;p) \cong 1 + p^2\zeta^2/2 \quad \text{(B4)}$$

The asymptotic approximations for large arguments are

$$\mathrm{Ch}\,(\zeta;p) \cong 2^{p-1}\zeta^p \quad \text{and} \quad \mathrm{Sh}\,(\zeta;p) \cong 2^{p-1}\zeta^p \quad \text{(B5)}$$

Both functions are related via

$$[\mathrm{Ch}\,(\zeta;p)]^2 - [\mathrm{Sh}\,(\zeta;p)]^2 = 1 \quad \text{(B6)}$$

Addition theorems are obtained by use of the definition (B1)

$$\mathrm{Sh}\,(\zeta;p_1 + p_2) = \mathrm{Sh}\,(\zeta;p_1)\,\mathrm{Ch}\,(\zeta;p_2) + \mathrm{Ch}\,(\zeta;p_1)\,\mathrm{Sh}\,(\zeta;p_2) \quad \text{(B7)}$$
$$\mathrm{Ch}\,(\zeta;p_1 + p_2) = \mathrm{Ch}\,(\zeta;p_1)\,\mathrm{Ch}\,(\zeta;p_2) + \mathrm{Sh}\,(\zeta;p_1)\,\mathrm{Sh}\,(\zeta;p_2) \quad \text{(B8)}$$

For $p_1 = p - 1$, $p_2 = 1$, $\mathrm{Sh}\,(\zeta;1) = \zeta$, $\mathrm{Ch}\,(\zeta;1) = \sqrt{1 + \zeta^2}$ (B7) and (B8) lead to

$$\sqrt{1 + \zeta^2}\,\mathrm{Sh}\,(\zeta;p) = \mathrm{Sh}\,(\zeta;p - 1) + \zeta\,\mathrm{Ch}\,(\zeta;p) \quad \text{(B9)}$$

The inversions of the functions are given by

$$\mathrm{Sh}\,(\zeta;p) = \eta \quad \Leftrightarrow \quad \zeta = \mathrm{Sh}\,(\eta;1/p) \quad \text{(B10)}$$

$$\mathrm{Ch}\,(\zeta;p) = \eta \quad \Leftrightarrow \quad |\zeta| = \mathrm{Sh}\left(\sqrt{\eta^2 - 1};1/p\right) \quad \text{(B11)}$$

If we replace in (B1) $\zeta \to \sinh\zeta$ it follows $\omega \to \exp\zeta$ and thus $\mathrm{Sh}\,(\sinh\zeta;p) = \sinh\,(p\zeta)$. In other words

$$\mathrm{Sh}\,(\zeta;p) = \sinh\,(p\,\mathrm{arcsinh}\zeta) = \mathrm{Sh}\,(\sinh p;\mathrm{arcsinh}\zeta) \quad \text{(B12)}$$
$$\mathrm{Ch}\,(\zeta;p) = \cosh\,(p\,\mathrm{arcsinh}\zeta) = \mathrm{Ch}\,(\sinh p;\mathrm{arcsinh}\zeta) \quad \text{(B13)}$$

Thus for small ζ it holds

$$\text{Sh}\,(\zeta; p) \cong \sinh\left(p\left(\zeta - \zeta^3/6 + 3\zeta^5/40\right)\right) \to \sinh\left(p\zeta\right) \quad \text{(B14)}$$

$$\text{Ch}\,(\zeta; p) \cong \cosh\left(p\left(\zeta - \zeta^3/6 + 3\zeta^5/40\right)\right) \to \cosh\left(p\zeta\right) \quad \text{(B15)}$$

This explains the similarity with the hyperbolic functions. For $\zeta < p^{-1/3}/4$ the difference between $\text{Ch}\,(\zeta; p)$ and $\cosh\left(p\,\zeta\right)$ is smaller than 0.26% and the difference between $\text{Sh}\,(\zeta; p)$ and $\sinh\left(p\,\zeta\right)$ is smaller than 1%.

REFERENCES

1. Nachtigal, D. and G. Bergmann, "Multi-pole magnetic encoders for active speed-measurement systems," *SAE-paper*, Paper No. 1999-01-3402, *Proc. of the 17th Annual Brake Colloquium & Engineering Display (SAE Proc.)*, 349, 53–58, Oct. 1999.

2. Saito, H., M. Kume, S. Kawamura, and O. Shimizu, "Wheel rotation sensor for use in a navigation/location system," *Sumitomo Electric Technical Review*, No. 28, 241–247, Jan. 1989.

3. Miyashita, K., T. Takahashi, and M. Yamanaka, "Features of a magnetic rotary encoder," *IEEE Trans. Magn.*, Vol. 23, No. 5, 2182–2184, Sept. 1987.

4. Kikuchi, Y., F. Nakamura, H. Wakiwaka, and H. Yamada, "Index phase output characteristics of magnetic rotary encoder using a magneto-resistive element," *IEEE Trans. Magn.*, Vol. 33, No. 5, 3370–3372, Sept. 1997.

5. Kikuchi, Y., F. Nakamura, H. Wakiwaka, and H. Yamada, "Consideration of magnetization and detection on magnetic rotary encoder using finite element method," *IEEE Trans. Magn.*, Vol. 33, No. 2, 2159–2162, Mar. 1997.

6. Campbell, P., "Miniature magnetic encoder," *Machine Design*, 105–108, Mar. 8, 1990.

7. Campbell, P., "Magnetic encoding technology," *Motor-Con Proceedings*, 211–219, Apr. 1987.

8. Kafader, U., "Für anspruchsvolle antriebstechnik," MegaLink, Vol. 10, 55–57, Oct. 2001.

9. Bancel, F. and G. Lemarquand, "Three-dimensional analytical optimization of permanent magnets alternated structure," *IEEE Trans. Magn.*, Vol. 34, No. 1, 242–247, Jan. 1998.

10. Bancel, F., "Magnetic nodes," *J. Phys. D: Appl. Phys.*, Vol. 32, 2155–2161, 1999.

11. Liu, W. Z., C. Y. Xu, and Z. Y. Ren, "Research of the surface magnetic field of multi-pole magnetic drum of

magnetic encoder," *Int'l Conf. Sensors and Control Techniques (ICSC2000), Proceedings of SPIE*, D.-S. Jiang and A.-B. Wang (eds.), Vol. 4077, 288–291, 2000.

12. Furlani, E. P., S. Reznik, and A. Kroll, "A three-dimensional field solution for radially polarized cylinders," *IEEE Trans. Magn.*, Vol. 31, No. 1, 844–851, Jan. 1995.

13. Furlani, E. P., "A three-dimensional field solution for axially-polarized multipole discs," *J. Magn. Magn. Mat.*, Vol. 135, 205–214, 1994.

14. Ravaud, R. and G. Lemarquand, "Magnetic field created by a uniformly magnetized tile permanent magnet," *Progress In Electromagnetics Research B*, Vol. 24, 17–32, 2010.

15. Ravaud, R., G. Lemarquand, V. Lemarquand, and C. Depollier, "Magnetic field produced by a tile permanent magnet whose polarization is both uniform and tangential," *Progress In Electromagnetics Research B*, Vol. 13, 1–20, 2009.

16. Ravaud, R. and G. Lemarquand, "Analytical expression of the magnetic field created by tile permanent magnets tangentially magnetized and radial currents in massive disks," *Progress In Electromagnetics Research B*, Vol. 13, 309–328, 2009.

17. Forrester, A. T. and J. Busnardo-Neto, "Magnetic fields for surface containment of plasmas," *J. Appl. Phys.*, Vol. 47, No. 9, 3935–3941, Sept. 1976.

18. Viana, R. L. and I. L. Caldas, "Comments on the magnetic field generated by an infinite current grid," *Eur. J. Phys.*, Vol. 12, 293–296, Dec. 1991.

19. Da Silva, E. C., I. L. Caldas, and R. L. Viana, "Ergodic magnetic limiter for the TCABR," *Brazilian J. Phys.*, Vol. 32, No. 1, 39–45, Jan. 2002.

20. Leung, K. N., N. Hershkowitz, and K. R. MacKenzie, "Plasma confinement by localized cusps," *Phys. Fluids*, Vol. 19, 1045–1053, 1976.

21. Nihei, H., "Analytic expressions of magnetic multipole field generated by a row of permanent magnets," *Jap. J. Appl. Phys.*, Vol. 29, No. 9, 1831–1832, Sept. 1990.

22. Ozeretskovskiy, V., "Calculation of two-dimensional nonperiodic multipole magnetic systems," *Sov. J. Commun. Techn. and Electr.*, Vol. 36, No. 8, 81–92, Aug. 1991.

23. Grinberg, E., "On determination of properties of some potential fields," Applied Magnetohydrodynamics, Reports of the Physics Inst. Riga, Vol. 12, 147–154, 1961.

24. Avilov, V. V., "Electric and magnetic fields for the riga plate," Internal Report FZR Forschungszentrum Rossendorf, Dresden, Germany, 1998. Published in a report by E. Kneisel, "Numerische und experimentelle untersuchungen zur grenzschichtbeeinflussung in schwach leitfähigen flüssigkeiten," Nov. 24, 2003, http://www.hzdr.de/FWS/FWSH/Mutschke/kleinerbeleg.pdf.

25. De Visschere, P., "An exact two-dimensional model for a periodic circular array of head-to-head permanent magnets," *J. Phys. D: Appl. Phys.*, Vol. 38, 355–362, 2005.

26. Wang, R., M. Kamper, K. Westhuizen, and J. Gieras, "Optimal design of a coreless stator axial flux permanent-magnet generator," *IEEE Trans. Magn.*, Vol. 41, No. 1, 55–64, Jan. 2005.

27. Furlani, E. P. and M. A. Knewtson, "A three-dimensional field solution for permanent-magnet axial-field motors," *IEEE Trans. Magn.*, Vol. 33, No. 3, 2322–2325, May 1997.

28. Gridnev, A. I., N. A. Kelin, N. I. Klevets, et al., "Synthesis and optimization of rods made of high-coercivity permanent magnets and systems for magnetization," *Izv. AN SSSR. Ser. Energetika i Transport*, No. 6, 1987.

29. Jackson, J. D., *Classical Electrodynamics*, 2nd German Edition, 219, 5.79, Walter de Gruyter, Berlin, New York, 1982, ISBN 3-11-009579-3.

30. Ravaud, R., G. Lemarquand, V. Lemarquand, and C. Depollier, "The three exact components of the magnetic field created by a radially magnetized tile permanent magnet," *Progress In Electromagnetics Research*, Vol. 88, 307–319, 2008.

31. Smythe, W. R., "Current images in plane face," *Static and Dynamic Electricity*, 3rd edition, Chapter 7.23, Taylor & Francis, 1989, ISBN 0-89116-917-2.

32. Hansen, E. R., *A Table of Series and Products*, 271, 41.2.16, Prentice Hall, N.J., 1975.

33. Hansen, E. R., *A Table of Series and Products*, 271, 41.2.14, Prentice Hall, N.J., 1975,

34. Ausserlechner, U., "Vorrichtung und verfahren zum erzeugen eines logischen ausgangssignals," German Patent Application DE 10214524, Apr. 2002.

35. Becker/Sauter, *Theorie der Elektrizität*, 21st edition, Vol. 1, 112, 5.4.22, B. G. Teubner, Stuttgart, 1973.

36. Arfken, G., *Mathematical Methods for Physicists*, 3rd edition, 618, Academic Press, San Diego, 1985.

37. Furlani, E. P., "Formulas for the force and torque of axial couplings," *IEEE Trans. Magn.*, Vol. 29, No. 5, 2295–2301, Sept. 1993.

38. Furlani, E. P., "A two-dimensional analysis for the coupling of magnetic gears," *IEEE Trans. Magn.*, Vol. 33, No. 3, 2317–2321, May 1997.

39. Furlani, E. P., "Analytical analysis of magnetically coupled multipole cylinders," *J. Phys. D: Appl. Phys.*, Vol. 33, 28–33, 2000.

40. Ravaud, R. and G. Lemarquand, "Magnetic couplings with cylindrical and plane air gaps: Influence of the magnet polarization direction," *Progress In Electromagnetics Research B*, Vol. 16, 333–349, 2009.

41. Ravaud, R., G. Lemarquand, V. Lemarquand, and C. Depollier, "Torque in PM couplings: Comparison of uniform and radial magnetization," *J. Appl. Phys.*, Vol. 105, 053904, 2009, DOI: 10.1063/1.3074108.

42. Ravaud, R., G. Lemarquand, V. Lemarquand, and C. Depollier, "Permanent magnet couplings: Field and torque three-dimensional expressions based on the coulombian model," *IEEE Trans. Magn.*, Vol. 45, No. 4, 1950–1964, 2009.

43. Huang, D. R., G.-J. Chiou, Y.-D. Yao, and S.-J. Wang, "Effect of magnetization profiles on the torque of magnetic coupling," *J. Appl. Phys.*, Vol. 76, No. 10, 6862–6864, Nov. 15, 1994.

44. Yao, Y. D., D. R. Huang, C. C. Hsieh, D. Y. Chiang, S. J. Wang, and T. F. Ying, "The radial magnetic coupling studies of perpendicular magnetic gears," *IEEE Trans. Magn.*, Vol. 32, No. 5, 5061–5063, Sept. 1996.

45. Yao, Y. D., G. J. Chiou, D. R. Huang, and S. J. Wang, "Theoretical computations for the torque of magnetic coupling," *IEEE Trans. Magn.*, Vol. 31, No. 3, 1881–1884, May 1995.

46. Tsamakis, D., M. Ioannides, and G. Nicolaides, "Torque transfer through plastic bonded Nd2Fe14B magnetic gear system," *J. Alloys Compounds*, Vol. 241, 175–179, 1996.

47. Hansen, E. R., *A Table of Series and Products*, Prentice Hall, N.J., 1975.

48. Ryshik, I. M. and I. S. Gradstein, *Tables of Series, Products, and Integrals*, VEB Deutscher Verlag der Wissenschaften, 34, 1.392, Berlin, 1957.